Journal of The Electrochemical Society, **166** (8) A1380-A1392 (2019)
0013-4651/2019/166(8)/A1380/13/$38.00 © The Electrochemical Society

Full Homogenized Macroscale Model and Pseudo-2-Dimensional Model for Lithium-Ion Battery Dynamics: Comparative Analysis, Experimental Verification and Sensitivity Analysis

Harikesh Arunachalam and Simona Onori [z]

Department of Energy Resources Engineering, Stanford University, Stanford, California 94305, USA

Control-oriented models based on electrochemistry have conventionally been evaluated and designed from the Doyle-Fuller-Newman (DFN) macroscale model. However, the DFN model is susceptible in predicting battery response under certain operating conditions since it is an approximate representation of pore-scale dynamics. This work shows the limitations of the DFN model in predicting voltage response at high temperatures of cell operation. A full homogenized macroscale (FHM) model, developed in previous research, is shown to overcome these limitations. Results indicate that the predictability of the DFN model deteriorates when trying to predict the voltage response at low state of charge for high temperature of operation under 1 C-rate discharge. The influence of parameters on the model states and output is investigated as a means to address parameter identifiability issues, for which, we formulate and resolve sensitivity functions for the partial differential equations (PDEs) of the FHM model. Results show that parameter identifiability is dependent on the battery state of charge.
 [DOI: 10.1149/2.0051908jes]

Manuscript submitted October 24, 2018; revised manuscript received April 8, 2019. Published April 25, 2019.

To address sustainable transportation concerns, the last decade has seen enormous strides in battery technology and the adoption of lithium-ion batteries in vehicular applications.[1] Despite the decreasing cost of lithium-ion battery packs over the years,[2] obstacles to widespread adoption of electrified vehicles still remain in terms of safety, performance degradation from aging, and lack of a comprehensive understanding of battery behavior under diverse operating conditions.[3] At the *pore* scale, lithium transport is modeled using first principles of mass and charge conservation.[4] However, their numerical complexity renders them impractical as a predictive tool at the system level. On the other hand, macroscopic models that describe lithium transport using averaged mass and charge transport equations are particularly appealing for developing control and estimation strategies.

The Doyle-Fuller-Newman (DFN) macroscale model[5] has been at the forefront for the electrochemical models used today. The inception of this model came at a time when lithium-ion technology was at a nascent phase and primarily targeted for portable electronic applications. Gradually, lithium-ion batteries demonstrated the potential for enhancing electrification in the transportation sector[6] due to lowering costs and energy density higher than other energy storage devices. For small-scale consumer electronics applications, battery degradation does not constitute a significant concern due to the short device lifetime and reasonable costs associated with battery replacement. However, understanding these mechanisms has become very crucial in large-scale, cost-intensive battery systems for long-term applications such as electric vehicles (8-10 years) and even more so for grid energy storage (20-30 years).

There has been sufficient evidence[7–11] to indicate a lack of predictability of the DFN model at high temperatures, low state-of-charge (SOC), over battery aging, and at high C-rates of operation. These are very important aspects to address in automotive lithium-ion batteries. Simplified[12,13] and reduced-order[14,15] formulations of the DFN model are conducive for state estimation and control development. However, these models factor a certain loss of physical intuition due to their diminished complexity. Their predictability, at best, is limited to the accuracy of the DFN model. Different studies[16–18] that validate the performance of such models restrict the battery operation to moderate temperatures, moderate to high C-rates, and low current rates of charge/discharge. As a result, the performance of such control-oriented models very likely won't reflect real-world battery response.

In Ref. 19, we compared the performance of the DFN model and a full homogenized macroscale (FHM) model which was rigorously derived using mathematical homogenization.[20] The parameters of the two models were independently identified, and averaged values of the common model parameters were used during the comparison studies. In this publication, we perform a simultaneous identification of the common model parameters using a combined cost function. This study is conducted on 18650 cylindrical lithium-ion cells with graphite anode and nickel manganese cobalt oxide (NMC) cathode.

Further, we formulate partial differential sensitivity equations for the FHM model and resolve them to obtain sensitivity functions. These functions provide first-order estimates of the impact of variation of effective diffusion ($D_{s,j}^{eff}$), reaction rate (k_j^*), and electrode saturation concentration ($c_{s,max,j}$) parameters on the concentration states, $\bar{c}_s$ and $\bar{c}_e$, respectively and voltage output. The foundation of this approach is based on a procedure in Ref. 21 that was originally designed for the states of a model defined by ordinary differential equations. In Ref. 22, a similar approach was used to study the effect of the parameters of an estimator, designed using a single particle model, on the system estimates. The novel contribution of this work is to formulate and resolve sensitivity equations for the states of a model defined by a system of non-linear coupled partial differential equations (PDEs).

This work is motivated by the need to understand limitations of two macroscale models and to provide an alternate modeling tool, such as the FHM model, to overcome DFN model limitations when design objectives require. This paper is structured as follows: DFN and FHM Models: Finite Element Approach section reviews the governing equations of the two models. Model Parameter Identification section outlines the parameter identification studies using an integrated co-simulation framework involving COMSOL Multiphysics and MATLAB. Results from parameter identification and model validation using multiple experimental data sets are presented in Results section. Investigation of the Arrhenius behavior of the diffusion and reaction rate parameters section investigates whether the identified diffusion and reaction rate transport parameters of the two models follow an Arrrhenius-type of relationship with temperature. A sensitivity study to assess the influence of model parameters on the output voltage is elaborated in Sensitivity Analysis of the FHM Model section. Appendices A and B supplement the discussion provided in Sensitivity Analysis of the FHM Model section. Finally, Conclusion section summarizes the conclusions of this paper.

DFN and FHM Models: Finite Element Approach

The mass and charge transport equations of the DFN[23] and the FHM[20] models are summarized in Table I. n, s, and p represent the anode, separator, and cathode, respectively. This section summarizes the governing equations, boundary conditions, and initial conditions of the DFN and FHM models. We refer the reader to Ref. 24 for a detailed comparison analysis of the transport equations of the two models. There are two fundamental differences between the DFN and

[z]E-mail: sonori@stanford.edu

Table I. Transport equations of the DFN and FHM battery models.

DFN Model	FHM Model
Electrode Mass Transport Equation; $j = (n, p)$	
$\frac{\partial c_{s,j}(x,r,t)}{\partial t} = \frac{D_{s,j}}{r^2}\left(r^2 \frac{\partial c_{s,j}(x,r,t)}{\partial r}\right)$	$\frac{\partial \bar{c}_{s,j}}{\partial t} = D_{s,j}^{eff} \frac{\partial^2 \bar{c}_{s,j}}{\partial x^2} - \frac{1}{F} J_{Li,j}(x,t)$
Electrolyte Mass Transport Equation; $j = (n, s, p)$	
$\eta_{e,j} \frac{\partial \bar{c}_{e,j}(x,t)}{\partial t} = \frac{\partial}{\partial x}\left(D_{e,j}^{eff} \frac{\partial \bar{c}_{e,j}(x,t)}{\partial x}\right) + \frac{(1-t_+)}{F} J_{Li,j}(x,t)$	$\eta_{e,j} \frac{\partial \bar{c}_{e,j}}{\partial t} = D_{e,j}^{eff} \frac{\partial^2 \bar{c}_{e,j}}{\partial x^2} + \frac{1}{F} J_{Li,j}(x,t) + \frac{RTt_+^2}{F^2} K_{e,j}^{eff} \frac{\partial^2 \ln \bar{c}_{e,j}}{\partial x^2} + \frac{t_+}{F} K_{e,j}^{eff} \frac{\partial^2 \bar{\phi}_{e,j}}{\partial x^2}$
Electrode Charge Transport Equation; $j = (n, p)$	
$K_{s,j}^{eff} \frac{\partial^2 \bar{\phi}_{s,j}(x,t)}{\partial x^2} = J_{Li,j}(x,t)$	$K_{s,j}^{eff} \frac{\partial^2 \bar{\phi}_{s,j}}{\partial x^2} = J_{Li,j}(x,t)$
Electrolyte Charge Transport Equation; $j = (n, s, p)$	
$-K_{e,j}^{eff} \frac{\partial^2 \bar{\phi}_{e,j}(x,t)}{\partial x^2} - \frac{2K_{e,j}^{eff}(x,t)RT(1-t_+)}{F} \frac{\partial^2 ln \bar{c}_{e,j}}{\partial x^2} = J_{Li,j}(x,t)$	$\frac{RTt_+}{F} K_{e,j}^{eff} \frac{\partial^2 \ln \bar{c}_{e,j}}{\partial x^2} + K_{e,j}^{eff} \frac{\partial^2 \bar{\phi}_{e,j}}{\partial x^2} = -J_{Li,j}(x,t)$
Intercalation Current Density; $j = (n, p)$	
$J_{Li,j}(x,t) = a_j k_j \cdot \sqrt{c_{s,surf,j}} \cdot \sqrt{\left(c_{s,max,j} - c_{s,surf,j}\right)} \cdot \sqrt{\bar{c}_{e,j}(x,t)}$ $\cdot 2 \sinh\left[\frac{0.5F}{RT}\left(\bar{\phi}_{s,j} - \bar{\phi}_{e,j} - U_{0,j}\right)\right]; J_{Li,s}(x,t) = 0$	$J_{Li,j}(x,t) = k_j^* \cdot \sqrt{\bar{c}_{e,j} \cdot \bar{c}_{s,j}} \cdot \sqrt{\left(1 - \frac{\bar{c}_{s,j}}{c_{s,max,j}}\right)}$ $\cdot 2 \sinh\left(\frac{F}{2RT}\left[\bar{\phi}_{s,j} - \bar{\phi}_{e,j} - U_{0,j}\right]\right); J_{Li,s}(x,t) = 0$

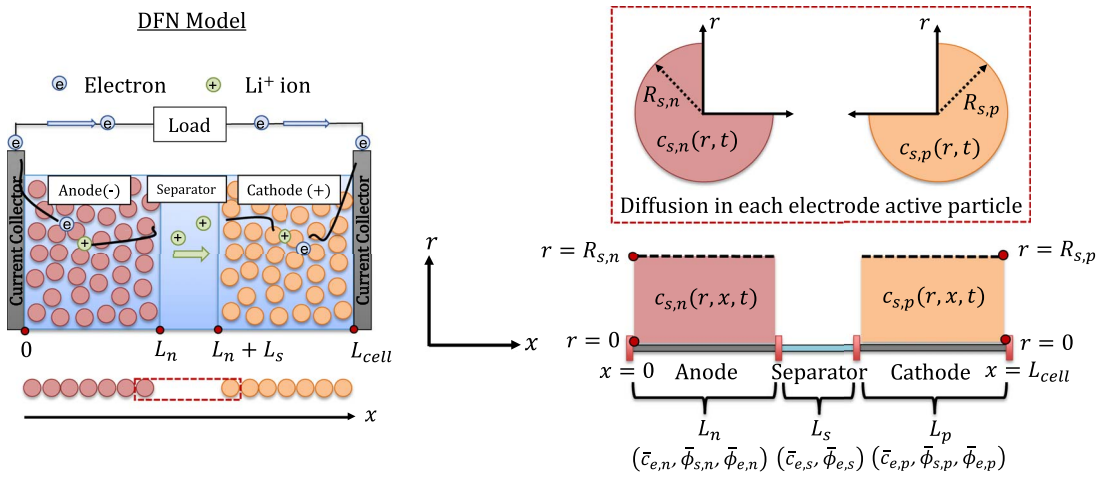

Figure 1. (a) The DFN model assumes that the electrodes are composed of spherical active particles. The effective ionic properties are determined empirically without considering the particle morphology. (b) Electrode concentration c_s is resolved in a *pseudo* radial direction, and the variables $\bar{\phi}_s$, $\bar{c}_e$, and $\bar{\phi}_e$ are resolved along the direction of electrode thickness.

the FHM models: a) the resolution of diffusion in the electrode using an averaged mass transport equation in the FHM model as opposed to a pseudo radial direction in the DFN model by assuming spherical active particles, and b) incorporating the effect of electromigration and diffusion in the electrolyte mass transport equation of the FHM model as opposed to only diffusion in the DFN model.

The DFN Model.—As illustrated in Fig. 1, the DFN model is a *pseudo two-dimensional* model since the electrolyte mass variable, $\bar{c}_e$, the electrolyte charge variable, $\bar{\phi}_e$, and the electrode charge variable, $\bar{\phi}_s$, are resolved in the direction perpendicular to the current collectors (1-D model), x, while electrode mass variable, c_s, is resolved in a *pseudo* radial direction, r, from the center to the surface of each active particle.

The boundary conditions of the variables $\bar{\phi}_s$, $\bar{\phi}_e$, and $\bar{c}_e$ of the DFN model are summarized in Table II. The variable c_s is resolved in r and x in the anode and the cathode, and its boundary conditions are:

$$\left.\frac{\partial c_{s,j}}{\partial r}\right|_{r=0} = 0 \quad \text{and} \quad D_{s,j} \left.\frac{\partial c_{s,j}}{\partial r}\right|_{r=R_{s,j}} = -\frac{J_{Li,j}}{a_j \cdot F}, \quad j = \{n, p\}. \quad [1]$$

The initial conditions for the variables of the DFN model are summarized in Table III. The non-linear PDEs of the model are coupled through the intercalation current density. In addition to this coupling, the charge conservation equation in the electrolyte consists of both the electrolyte concentration and potential variables.

The FHM Model.—As illustrated in Fig. 2, the coupled non-linear PDEs of the FHM model are resolved in the direction perpendicular to the current collectors. Both the mass and charge conservation

Table II. Boundary conditions of the DFN model variables $\bar{\phi}_s$, $\bar{\phi}_e$, and $\bar{c}_e$.

Variable	Location: $x = 0$	Location: $x = L_n$	Location: $x = L_n + L_s$	Location: $x = L_{cell}$
$\bar{\phi}_s$	$\bar{\phi}_{s,n} = 0$	$\frac{\partial \bar{\phi}_{s,n}}{\partial x} = 0$	$\frac{\partial \bar{\phi}_{s,p}}{\partial x} = 0$	$K_{s,p}^{eff} \frac{\partial \bar{\phi}_{s,p}}{\partial x} = -\frac{I_{app}}{A_{cell}}$
$\bar{\phi}_e$	$\frac{\partial \bar{\phi}_{e,n}}{\partial x} = 0$	Not required due to continuity	Not required due to continuity	$\frac{\partial \bar{\phi}_{e,p}}{\partial x} = 0$
$\bar{c}_e$	$\frac{\partial \bar{c}_{e,n}}{\partial x} = 0$	Not required due to continuity	Not required due to continuity	$\frac{\partial \bar{c}_{e,p}}{\partial x} = 0$

Table III. Initial conditions of the four variables of the DFN model.

Variable	Anode	Separator	Cathode
$\bar{\phi}_s$	$\bar{\phi}_{s,n} = 0$	Not applicable	$\bar{\phi}_{s,p}(t=0) = \left[U_{0,p}(x_{p,init}) - U_{0,n}(x_{n,init})\right]$
$\bar{\phi}_e$	$\bar{\phi}_{e,n}(t=0) = 0$	$\bar{\phi}_{e,sep}(t=0) = 0$	$\bar{\phi}_{e,p}(t=0) = 0$
c_s	$c_{s,n}(t=0) = x_{n,init} \cdot c_{s,max,n}$	Not applicable	$c_{s,p}(t=0) = x_{p,init} \cdot c_{s,max,p}$
$\bar{c}_e$	$\bar{c}_{e,n}(t=0) = c_{e,init}$	$\bar{c}_{e,sep}(t=0) = c_{e,init}$	$\bar{c}_{e,p}(t=0) = c_{e,init}$

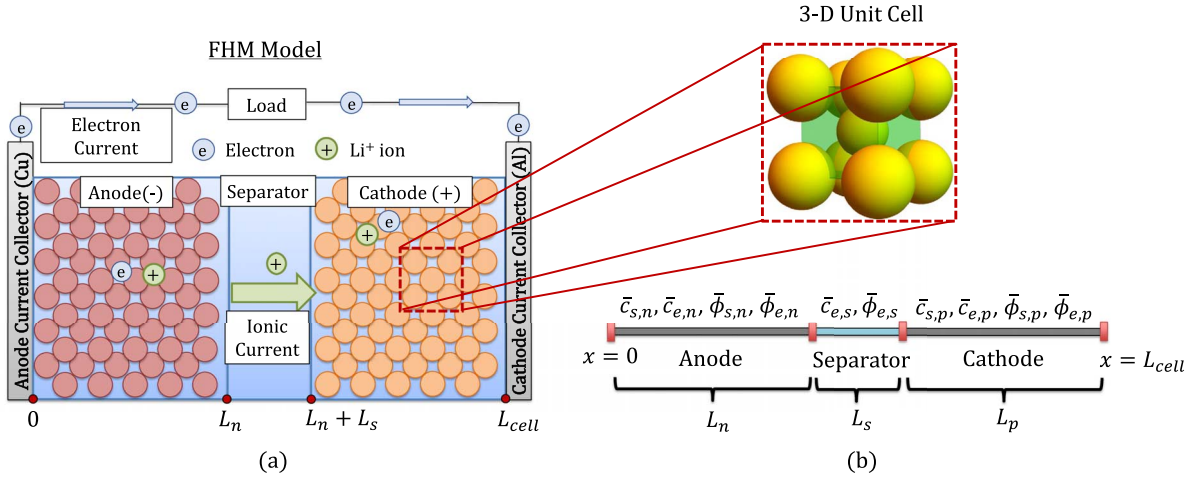

Figure 2. (a) The FHM model assumes that the electrodes are composed of spatially periodic unit cells. The effective ionic properties are determined by resolving a closure problem[24] in the unit cell of the electrode microstructure. (b) The implementation of the FHM model in 1-D is presented in this work, where the variables of the model are resolved along the direction of electrode thickness.

equations in the electrolyte phase consist of the electrolyte concentration and potential variables. The boundary and initial conditions of the FHM model variables $\bar{c}_s$, $\bar{\phi}_s$, $\bar{c}_e$, and $\bar{\phi}_e$ are summarized in Table IV and Table V, respectively.

General remarks.—The equations of the DFN and FHM models are resolved for an input current profile $I_{app}(t)$. The model-predicted voltage output, $V(t)$, is defined as:

$$V(t) = \bar{\phi}_s(L_{cell}, t) - \bar{\phi}_s(0, t) - R_c \cdot I_{app}(t) \quad [2]$$

Pore-scale electrolyte diffusion ($D_{e,j}$) and conductivity ($K_{e,j}$) coefficients as a function of concentration and temperature were obtained from Ref. 25. Effective diffusion and conductivity for the DFN model were obtained using the Bruggeman approach,[26] and by resolving the closure problem for the FHM model.[24] The radius of the active particles in the anode and cathode were kept constant at a value of 5 μm for both models. For the DFN model, a built-in fine mesh was utilized for discretization in the 1-D direction of electrode thickness, while a customized user-controlled mesh was utilized for the pseudo 2-D domain. The mesh settings utilized by Plett et al.[27] for the DFN model have been retained as is without any modifications. Since the equations of the FHM model are all resolved in 1-D, a built-in extremely fine mesh was utilized for discretization along the direction of electrode thickness.

Model Parameter Identification

In Ref. 28 the authors elaborate upon the implementation of the FHM model using COMSOL Multiphysics. To facilitate the comparison studies on the voltage prediction performance of the DFN and FHM models, we adapted the DFN model developed in the same software platform by Plett et al. This section details the identification studies conducted to determine the parameters of the two models using an integrated Matlab and COMSOL Multiphysics co-simulation framework.

For an elaborate description of the development and numerical implementation of the FHM model, the reader is referred to Ref. 28. The performance of both models were assessed using data acquired from

Table IV. Boundary conditions of FHM model variables $\bar{c}_s$, $\bar{\phi}_s$, $\bar{c}_e$, and $\bar{\phi}_e$.

Variable	Location: $x = 0$	Location: $x = L_n$	Location: $x = L_n + L_s$	Location: $x = L_{cell}$
$\bar{c}_s$	$\frac{\partial \bar{c}_{s,n}}{\partial x} = 0$	$D_{s,n}^{eff} \frac{\bar{c}_{s,n}}{\partial x} = -\frac{J_{Li,n}}{F \cdot L_n}$	$D_{s,p}^{eff} \frac{\bar{c}_{s,p}}{\partial x} = -\frac{J_{Li,p}}{F \cdot L_p}$	$\frac{\partial \bar{c}_{s,p}}{\partial x} = 0$
$\bar{\phi}_s$	$\bar{\phi}_{s,n} = 0$	$\frac{\partial \bar{\phi}_{s,n}}{\partial x} = 0$	$\frac{\partial \bar{\phi}_{s,p}}{\partial x} = 0$	$K_{s,p}^{eff} \frac{\partial \bar{\phi}_{s,p}}{\partial x} = -\frac{I_{app}}{A_{cell}}$
$\bar{c}_e$	$\frac{\partial \bar{c}_{e,n}}{\partial x} = 0$	Not required due to continuity	Not required due to continuity	$\frac{\partial \bar{c}_{e,p}}{\partial x} = 0$
$\bar{\phi}_e$	$\frac{\partial \bar{\phi}_{e,n}}{\partial x} = 0$	Not required due to continuity	Not required due to continuity	$\frac{\partial \bar{\phi}_{e,p}}{\partial x} = 0$

Table V. Initial conditions of the four variables of the FHM model.

Variable	Anode	Separator	Cathode
$\bar{\phi}_s$	$\bar{\phi}_{s,n} = 0$	Not applicable	$\bar{\phi}_{s,p}(t=0) = \left[U_{0,p}(x_{p,init}) - U_{0,n}(x_{n,init})\right]$
$\bar{\phi}_e$	$\bar{\phi}_{e,n}(t=0) = 0$	$\bar{\phi}_{e,sep}(t=0) = 0$	$\bar{\phi}_{e,p}(t=0) = 0$
$\bar{c}_s$	$\bar{c}_{s,n}(t=0) = x_{n,init} \cdot c_{s,max,p}$	Not applicable	$\bar{c}_{s,p}(t=0) = x_{p,init} \cdot c_{s,max,p}$
$\bar{c}_e$	$\bar{c}_{e,n}(t=0) = c_{e,init}$	$\bar{c}_{e,sep}(t=0) = c_{e,init}$	$\bar{c}_{e,p}(t=0) = c_{e,init}$

experiments conducted on 18650 cylindrical lithium-ion cells composed of graphite anode and NMC cathode. The specifications of the cells used in the experiments can be obtained from Ref. 29. Due to the lack of availability of information concerning the geometric thickness of the electrodes from the cell manufacturer, these parameters have also been included in the identification study. The details of the experimental work conducted for acquiring the data sets used in this study are elaborated in chapter 3 of Ref. 28.

The parameters of both models were identified using the particle swarm optimization (PSO) algorithm.[30] The vector of parameters for the DFN model is:

$$\theta_{DFN} = \left[L_n\, L_s\, L_p\, A_{cell}\, D_{s,n}\, D_{s,p}\, k_n\, k_p\, R_c\, x_{n,init}\, x_{p,init}\right.$$
$$\left. c_{s,max,n}\, c_{s,max,p}\, \eta_n\, \eta_p\, \eta_{e,n}\, \eta_{e,s}\, \eta_{e,p}\right]^T, \quad [3]$$

and the vector of parameters for the FHM model is:

$$\theta_{FHM} = \left[L_n\, L_s\, L_p\, A_{cell}\, D_{s,n}^{eff}\, D_{s,p}^{eff}\, k_n^*\, k_p^*\, R_c\, x_{n,init}\, x_{p,init}\right.$$
$$\left. c_{s,max,n}\, c_{s,max,n}\, \eta_n\, \eta_p\, \eta_{e,n}\, \eta_{e,s}\, \eta_{e,p}\right]^T \quad [4]$$

Figure 3 summarizes the co-simulation flowchart for the parameter identification study. Initial bounds for the model parameters were based on the values reported in Ref. 31. While it is true that parameter bounds can always be expanded to yield an optimum that neither coincides with their minimum (or) maximum values, these values may not be physically meaningful. For example, solid phase volume fraction cannot exceed 0.74, the maximum atomic packing factor possible. Given the lack of parameter information from the manufacturer, we have chosen to impose bounds that are physically meaningful rather than maximize them to facilitate the convenience of the identification process.

Experience[15,16] dictates that the parameters of the two models can be categorized into: a) geometric and stoichiometric parameters, and b) temperature-dependent parameters. The former category characterizes the design of a lithium-ion cell. Therefore, it is not justified to use different values for these parameters for different models, since in principle the should possess the same value. We propose a new improved two-layer identification approach to determining these parameters.

The first step is to minimize the RMS error in the model-predicted voltage response by identifying a common set of geometric and stoichiometric parameters. The cost function for Step 1 is:

$$M_{opt,1} = \left\{\frac{1}{N}\sum_{i=1}^{N}\left(V_m(i) - V_{FHM}(\theta_{FHM}; i)\right)^2 + \frac{1}{N}\sum_{i=1}^{N}\left(V_m(i) - V_{DFN}(\theta_{DFN}; i)\right)^2\right\}^{0.5}, \quad [5]$$

where V_m is the measured voltage, V_{FHM} and V_{DFN} are the model-predicted voltages from the FHM and DFN models, N is the total data samples, and i is the time index. The geometric and stoichiometric parameters is defined by the vector:

$$\theta_{opt,1} = \left[L_n\, L_s\, L_p\, A_{cell}\, x_{n,init}\, x_{p,init}\, c_{s,max,n}\, c_{s,max,n}\, \eta_n\, \eta_p\, \eta_{e,n}\, \eta_{e,s}\, \eta_{e,p}\right]^T \quad [6]$$

The identified values of the common parameters of the two models are summarized in Table VI. The optimization bounds were formulated based on prior values of the model parameters reported in literature.[31,32] It can be noted that the electrochemical parameter values reported are obtained from multiple sources, and are either assumed or estimated values. To the best of our knowledge, there are very rare instances where measured electrochemical parameters have

Table VI. The identification bounds and the identified values of the common DFN and FHM model parameters at the end of Step 1.

Parameter	Identification Bounds	Identified Value
L_n	$[45 \times 10^{-6}, 55 \times 10^{-6}]$	53.2×10^{-6}
L_s	$[20 \times 10^{-6}, 32 \times 10^{-6}]$	24.7×10^{-6}
L_p	$[35 \times 10^{-6}, 45 \times 10^{-6}]$	39.9×10^{-6}
$\eta_{s,n}$	[0.54, 0.66]	0.626
$\eta_{s,p}$	[0.50, 0.60]	0.574
$\eta_{e,n}$	[0.28, 0.36]	0.30
$\eta_{e,s}$	[0.35, 0.45]	0.35
$\eta_{e,p}$	[0.28, 0.36]	0.36
A_{cell}	[0.1006, 0.1120]	0.1037
R_c	[0.024, 0.036]	0.027
$x_{n,init}$	[0.75, 0.80]	0.7916
$x_{p,init}$	[0.31, 0.36]	0.3494
$c_{s,max,n}$	[26000, 31500]	27088
$c_{s,max,p}$	[45000, 50000]	48700

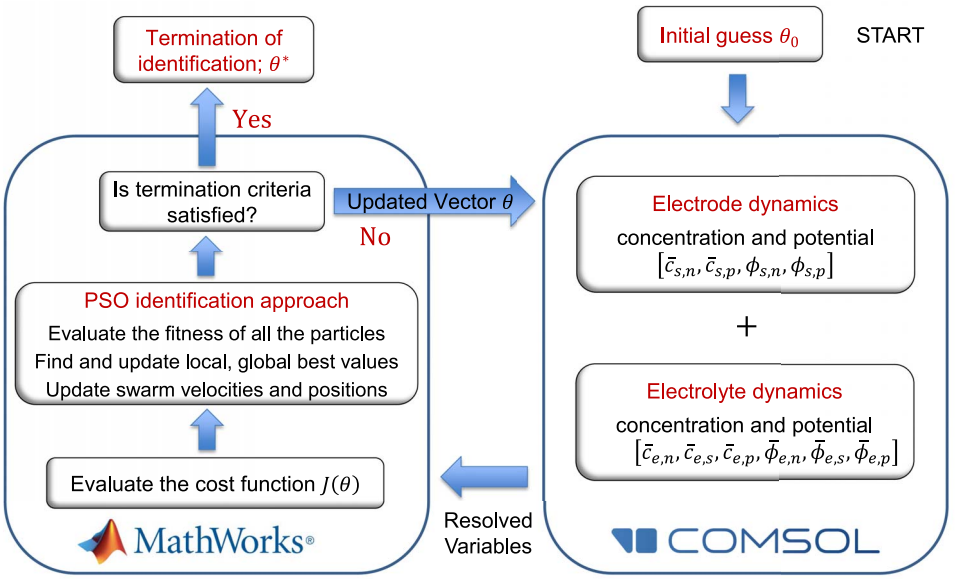

Figure 3. Flowchart describing the iterative process of model parameter identification of the FHM model in the co-simulation framework.

been inferred. Based on Table VI, it can be observed that the identified values of parameters $\eta_{e,s}$ and $\eta_{e,p}$ match their lower and upper bounds, respectively. The main reason for this result is that the terminal voltage is insensitive to changes in the values of such parameters, rendering their identification process a challenging task. We chose to leave the identified result rather than arbitrarily assigning a fixed value.

The identified values of the elements of the vector $\theta_{opt,1}$ at the end of Step 1 were used in both models without any further modifications for subsequent simulations. The second step is to minimize the RMS error in the model-predicted voltage response by identifying only the temperature-dependent parameters. The other temperature data sets were used, and the cost function for Step 2 is:

$$M_{opt,2} = \left\{ \frac{1}{N}\sum_{i=1}^{N}\left(V_m(i) - V_{FHM}(\theta_{5,FHM}; i)\right)^2 + \frac{1}{N}\sum_{i=1}^{N}\left(V_m(i) - V_{DFN}(\theta_{5,DFN}; i)\right)^2 \right\}^{0.5}, \quad [7]$$

where

$$\theta_{5,DFN} = \left[D_{s,n}\, D_{s,p}\, k_n\, k_p\, R_c\right]^T \quad \text{and} \quad \theta_{5,FHM} = \left[D_{s,n}^{eff}\, D_{s,p}^{eff}\, k_n^*\, k_p^*\, R_c\right]^T$$

for the DFN and FHM models, respectively.

The identification studies were setup using a population size of 200 swarms and 10 generations. The anode and cathode conductivity coefficients were maintained constant, since prior identification studies[33] deduced that they had no impact on the model-predicted voltage. Their values are obtained from literature[34] and kept the same for all the identification studies. The identification study using the co-simulation framework was conducted on a Dell Precision T5810 desktop computer with 32.0 GB RAM and Intel(R) Xeon(R) CPU E5-1650 v3 3.50 GHz processor.

Results.—The result of the identification studies are presented in Fig. 4. The percentage RMS error is given by:

$$\text{RMS Error} = \sqrt{\frac{1}{N}\sum_{i=1}^{N}\left(V_m(i) - V_{model}(\theta; i)\right)^2} \cdot \frac{100}{\text{mean}(V_m)}, \quad [8]$$

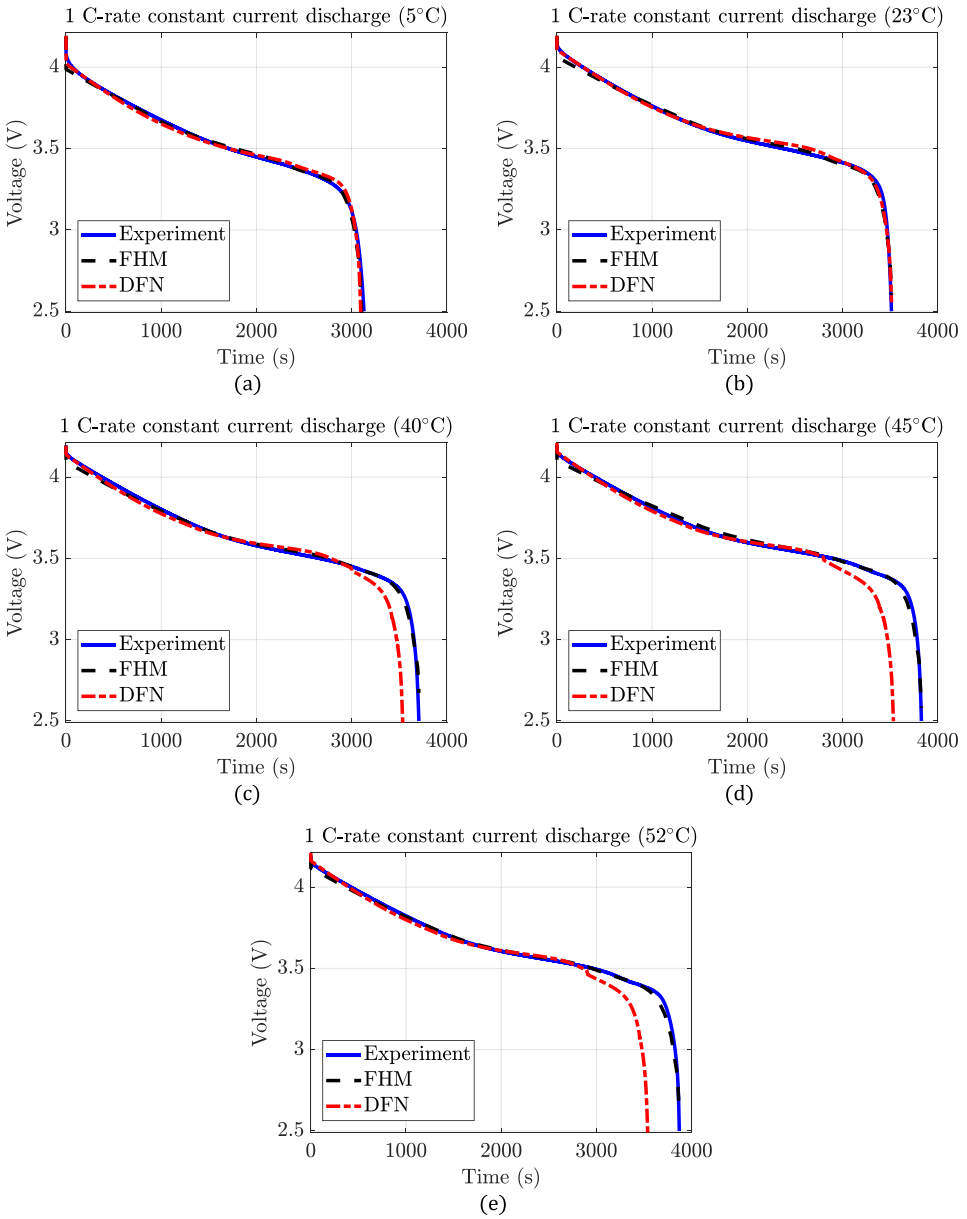

Figure 4. Performance of the DFN and FHM models against measured voltage from 1 C-rate discharge tests conducted at (a) 5°C, (b) 23°C, (c) 40°C, (d) 45°C, and (e) 52°C.

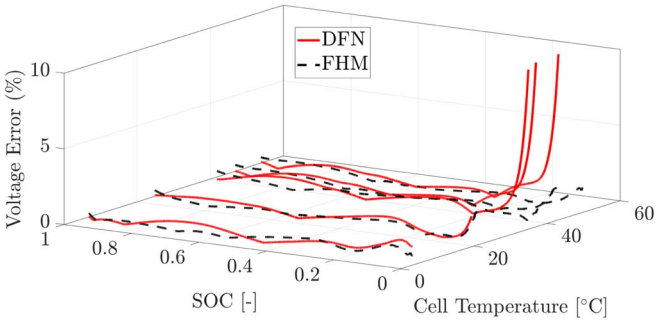

Figure 5. System level diagram representing the percentage error in the DFN and FHM model-predicted voltage with respect to experimental data as a function of SOC and temperature. The percentage voltage error was evaluated for the 1 C-rate constant current discharge data sets presented in this work.

where V_{model} is either V_{DFN} or V_{FHM}. The accuracy of the DFN degrades with increasing temperature, whereas the FHM model performs better than the DFN model at elevated temperatures. The voltage modeling error as a function of temperature and SOC for the identification data sets is illustrated in Fig. 5, where the normalized absolute value of the voltage error is calculated using the expression:

$$\%\ \text{Voltage Error} = \left|V_m(i) - V_{model}(\theta; i)\right| \cdot \frac{100 \cdot N}{\sum_{i=1}^{N} V_{exp}(i)}. \quad [9]$$

The SOC of the cell is calculated using coulomb counting. From the measured cell current, the cell SOC, $SOC(t)$, is determined as follows:

$$SOC(t) = SOC_{ini} - \frac{1}{Q_{cell}} \cdot \int_{t_0}^{t_f} I_{app}(t)dt\,, \quad [10]$$

where SOC_{ini} is the initial cell SOC; t_0 and t_f denote the beginning and end of cell discharge. For the capacity tests in discharge, $SOC_{ini} = 100\%$ and $t_0 = 0$ s.

The performance of both models was validated against constant current in discharge experimental data sets with C-rates of 1/20 and 15. The result of these validation studies are presented in Fig. 6, and the RMS error in voltage prediction for the DFN and FHM models are summarized in Table VII. An important assumption of the DFN model is lithium solid phase diffusion based on perfectly spherical active particles. Cell discharge is majorly dictated by anode concentration dynamics. At high temperature of battery operation, the concentration dynamics based on spherical particle diffusion likely over-predicts the rate of lithium depletion in the anode. This observation has been discussed earlier in Section 4.6 of Ref. 28.

Table VII. Percentage RMS error in the voltage prediction of the FHM and DFN models with respect to experimental measurements.

		RMS Error	
Reference	Data Set	DFN Model	FHM Model
Fig. C.4(a)	1 C-rate discharge at 5°C	0.68%	0.66%
Fig. C.4(b)	1 C-rate discharge at 23°C	0.55%	0.60%
Fig. C.4(c)	1 C-rate discharge at 40°C	2.26%	0.56%
Fig. C.4(d)	1 C-rate discharge at 45°C	2.59%	0.57%
Fig. C.4(e)	1 C-rate discharge at 52°C	2.59%	0.51%
Fig. C.6(a)	1/20 C-rate discharge at 23°C	0.88%	0.91%
Fig. C.6(b)	15 C-rate discharge at 23°C	2.28%	1.27%

The effective ionic transport properties of the DFN model do not consider information of the electrode morphology. Since we do not consider any fitting of electrolyte transport parameters, a certain loss of information can also affect the model accuracy. In Ref. 19,20, we have presented electrolyte phase diagrams to compare the time-scales associated with pore-scale transport processes: diffusion, electromigration, and reaction. Elevated temperatures and high C-rates of operation can lead to a scenario where diffusion is no longer the dominant transport mechanism. Under this scenario, the pore-scale is no longer well-mixed due to the formation of localized gradients. Then the error in the predictability of macroscale DFN-type models is no longer bounded with respect to its microscale counterpart.

Investigation of the Arrhenius behavior of the diffusion and reaction rate parameters.—An Arrhenius curve fitting approach was performed to determine the trend of behavior of the model parameters such as diffusion and reaction rate with respect to temperature. The results are shown for the DFN model in Fig. 7. The results from curve-fitting based on an Arrhenius-type relationship of diffusion and reaction rate of the two electrodes for the FHM model is shown in Fig. 8. The results from these figures indicate that the electrode diffusion coefficients of the two models follow the Arrhenius relationship closely. This behavior is also observed in the cathode reaction rate constants of both models. However, the same cannot be explicitly states with respect to the anode reaction rates. Regardless, relatively small changes in parameter values can influence the parameter variation trend toward an Arrhenius relationship. This will be investigated further as part of future work.

To the best of the authors' knowledge, there are no experimental measurements of reaction rates reported in literature. Studies[35,36]

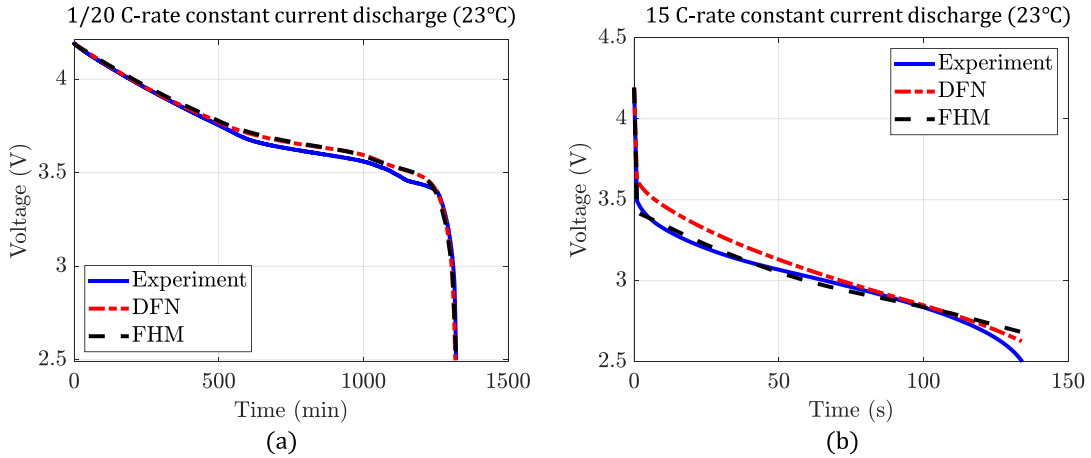

Figure 6. Validation of the performance of the DFN and FHM models against experimentally measured cell terminal voltage for (a) 1/20 C-rate and (b) 15 C-rate. These experiments were conducted at 23°C.

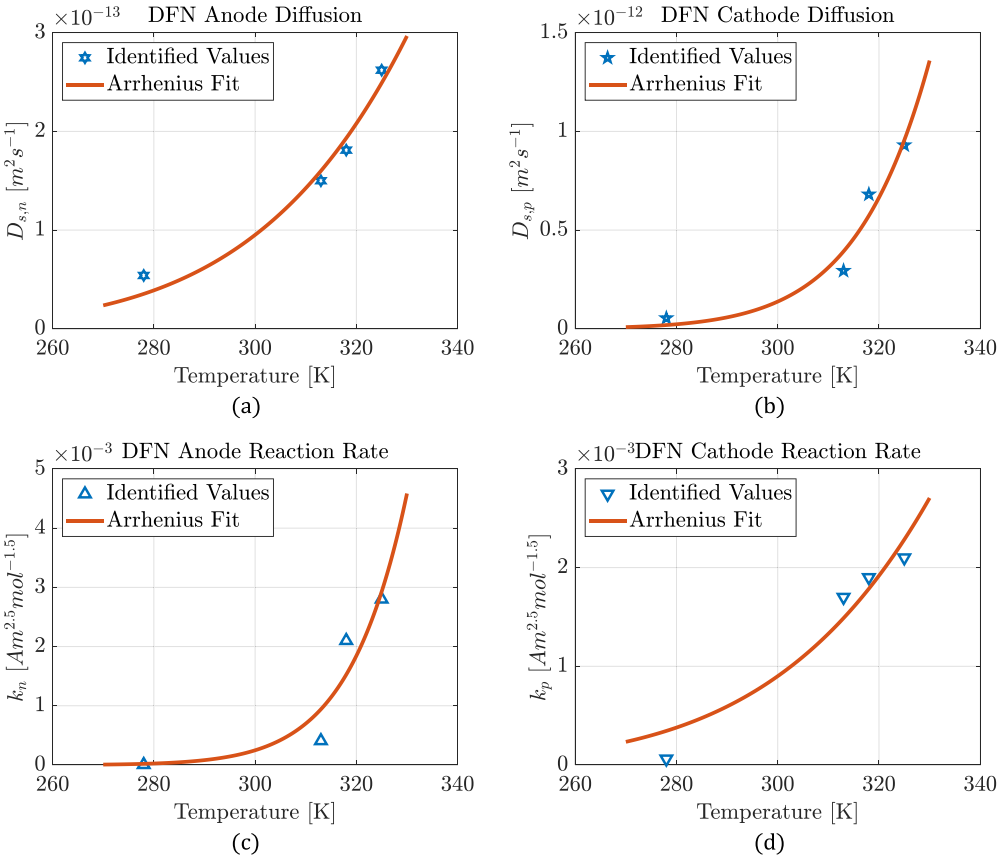

Figure 7. Comparison of the Arrhenius curve fit versus the identified DFN model parameters: (a) $D_{s,n}$, (b) $D_{s,p}$, (c) k_n, and (d) k_p.

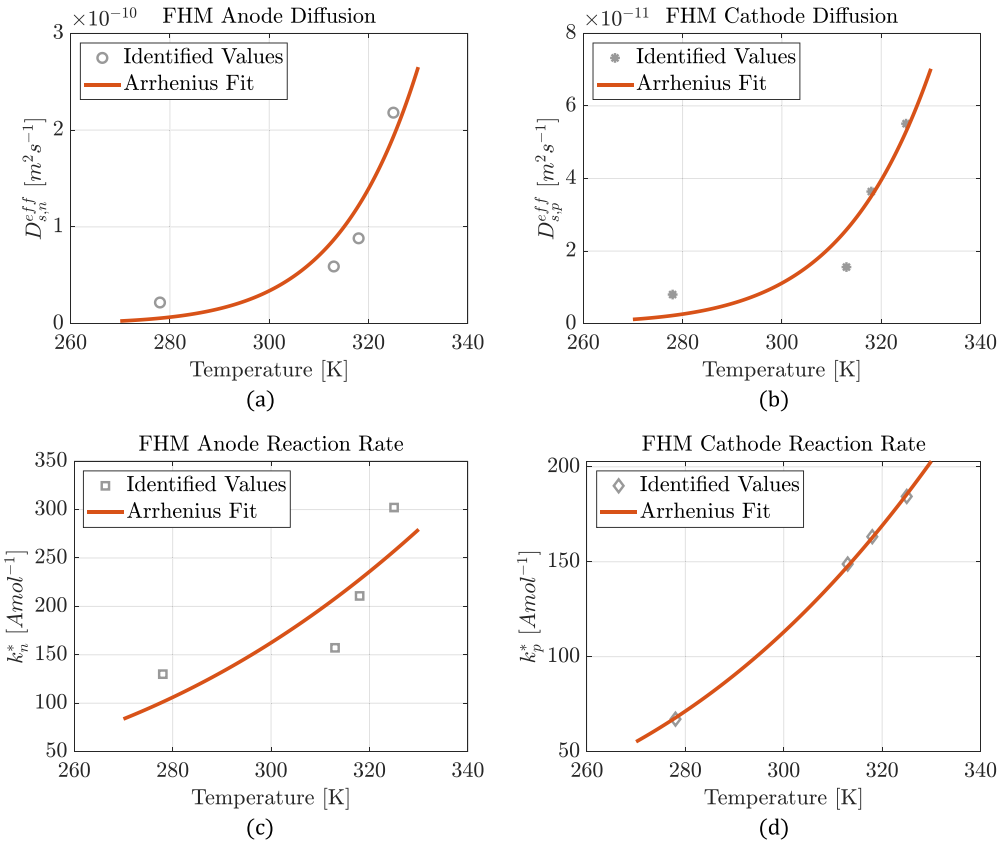

Figure 8. Comparison of the Arrhenius curve fit versus the identified FHM model parameters: (a) $D_{s,n}^{eff}$, (b) $D_{s,p}^{eff}$, (c) k_n^*, and (d) k_p^*.

Table VIII. Boundary conditions of the sensitivity variables $\frac{\partial \bar{c}_{s,j}}{\partial \theta_{i,j}}$ and $\frac{\partial \bar{c}_{e,j}}{\partial \theta_{i,j}}$.

Variable	Location: $x = \{0, L_{cell}\}$	Location: $x = \{L_n, L_n + L_s\}$
$\frac{\partial \bar{c}_{s,j}}{\partial D^{eff}_{s,j}}$	$\frac{\partial}{\partial x}\left(\frac{\partial \bar{c}_{s,j}}{\partial D^{eff}_{s,j}}\right) = 0$	$D^{eff}_{s,j}\frac{\partial}{\partial x}\left(\frac{\partial \bar{c}_{s,j}}{\partial D^{eff}_{s,j}}\right) = -\frac{\partial \bar{c}_{s,j}}{\partial x} - \frac{L_j}{F}\cdot\frac{\partial \bar{c}_{s,j}}{\partial D^{eff}_{s,j}}\cdot\frac{\partial J_{Li,j}}{\partial \bar{c}_{s,j}} - \frac{L_j}{F}\cdot\frac{\partial \bar{c}_{e,j}}{\partial D^{eff}_{s,j}}\cdot\frac{\partial J_{Li,j}}{\partial \bar{c}_{e,j}}$
$\frac{\partial \bar{c}_{e,j}}{\partial D^{eff}_{s,j}}$	$\frac{\partial}{\partial x}\left(\frac{\partial \bar{c}_{e,j}}{\partial D^{eff}_{s,j}}\right) = 0$	$\left(\frac{\partial \bar{\phi}_{e,j}}{\partial \bar{c}_{e,j}} + \frac{RTt_+}{F\bar{c}_{e,j}}\right)\cdot\frac{\partial}{\partial x}\left(\frac{\partial \bar{c}_{e,j}}{\partial D^{eff}_{s,j}}\right) = \frac{RTt_+}{F\bar{c}^2_{e,j}}\cdot\frac{\partial \bar{c}_{e,j}}{\partial x}\cdot\frac{\partial \bar{c}_{e,j}}{\partial D^{eff}_{s,j}}$
$\frac{\partial \bar{c}_{s,j}}{\partial k^*_j}$	$\frac{\partial}{\partial x}\left(\frac{\partial \bar{c}_{s,j}}{\partial k^*_j}\right) = 0$	$D^{eff}_{s,j}\frac{\partial}{\partial x}\left(\frac{\partial \bar{c}_{s,j}}{\partial k^*_j}\right) = -\frac{L_j}{F}\left[\frac{\partial \bar{c}_{s,j}}{\partial k^*_j}\cdot\frac{\partial J_{Li,j}}{\partial \bar{c}_{s,j}} + \frac{\partial \bar{c}_{e,j}}{\partial k^*_j}\cdot\frac{\partial J_{Li,j}}{\partial \bar{c}_{e,j}}\right.$ $\left. + 2\sqrt{\bar{c}_{e,j}\bar{c}_{s,j}\left(1-\frac{\bar{c}_{s,j}}{c_{s,max,j}}\right)}\cdot\sinh\left(\frac{F}{2RT}\left\{\bar{\phi}_{s,j} - \bar{\phi}_{e,j} - U_{0,j}\left(\frac{\bar{c}_{s,j}}{c_{s,max,j}}\right)\right\}\right)\right]$
$\frac{\partial \bar{c}_{e,j}}{\partial k^*_j}$	$\frac{\partial}{\partial x}\left(\frac{\partial \bar{c}_{e,j}}{\partial k^*_j}\right) = 0$	$\left(\frac{\partial \bar{\phi}_{e,j}}{\partial \bar{c}_{e,j}} + \frac{RTt_+}{F\bar{c}_{e,j}}\right)\cdot\frac{\partial}{\partial x}\left(\frac{\partial \bar{c}_{e,j}}{\partial k^*_j}\right) = \frac{RTt_+}{F\bar{c}^2_{e,j}}\cdot\frac{\partial \bar{c}_{e,j}}{\partial x}\cdot\frac{\partial \bar{c}_{e,j}}{\partial k^*_j}$
$\frac{\partial \bar{c}_{s,j}}{\partial c_{s,max,j}}$	$\frac{\partial}{\partial x}\left(\frac{\partial \bar{c}_{s,j}}{\partial c_{s,max,j}}\right) = 0$	$D^{eff}_{s,j}\frac{\partial}{\partial x}\left(\frac{\partial \bar{c}_{s,j}}{\partial c_{s,max,j}}\right) = -\frac{L_j}{F}\cdot\frac{\partial \bar{c}_{s,j}}{\partial c_{s,max,j}}\cdot\frac{\partial J_{Li,j}}{\partial \bar{c}_{s,j}} -$ $\frac{L_j}{F}\frac{\partial \bar{c}_{e,j}}{\partial c_{s,max,j}}\cdot\frac{\partial J_{Li,j}}{\partial \bar{c}_{e,j}} + \sqrt{\bar{c}_{e,j}\bar{c}_{s,j}\left(1-\frac{\bar{c}_{s,j}}{c_{s,max,j}}\right)}$ $\cdot\cosh\left(\frac{F}{2RT}\left\{\bar{\phi}_{s,j} - \bar{\phi}_{e,j} - U_{0,j}\left(\frac{\bar{c}_{s,j}}{c_{s,max,j}}\right)\right\}\right)\cdot\left(\frac{L_j k^*_j}{RT}\right)\cdot\frac{\partial U_{0,j}}{\partial c_{s,max,j}}$
$\frac{\partial \bar{c}_{e,j}}{\partial c_{s,max,j}}$	$\frac{\partial}{\partial x}\left(\frac{\partial \bar{c}_{e,j}}{\partial c_{s,max,j}}\right) = 0$	$\left(\frac{\partial \bar{\phi}_{e,j}}{\partial \bar{c}_{e,j}} + \frac{RTt_+}{F\bar{c}_{e,j}}\right)\cdot\frac{\partial}{\partial x}\left(\frac{\partial \bar{c}_{e,j}}{\partial c_{s,max,j}}\right) = \frac{RTt_+}{F\bar{c}^2_{e,j}}\cdot\frac{\partial \bar{c}_{e,j}}{\partial x}\cdot\frac{\partial \bar{c}_{e,j}}{\partial c_{s,max,j}}$

mostly reported diffusion coefficients as a function of the stoichiometric (lithiation) coefficient for a single temperature. However, temperature-based diffusion coefficients which were obtained from experimental characterization of NMC electrodes were reported in Refs. 37,38. These articles also reported that the diffusion coefficient increases with temperature following an Arrhenius relationship. It can be verified from Figures 7 and 8 that the values obtained from the identification studies in this work also exhibit the same trend as observed in literature.

Sensitivity Analysis of the FHM Model

Sensitivity analysis is a useful tool to understand the relationship between model parameters and model response. The information derived from these studies provides insights on parameter identifiability. Till date, there have been no studies reported in literature that examine the impact of parameter variation on the states of an electrochemical battery model.

Sensitivity information can be used to estimate which parameters are the most influential in affecting the behavior of the simulated output. Such information is crucial for experimental design and reduction of complex PDE non-linear models to design control-oriented models. In this section, we present this study for the FHM model by formulating a system of partial differential sensitivity equations from the governing PDEs, and resolve them along with the model equations. This is elaborated in the following subsections.

Sensitivity equations of the electrode.—The sensitivity of the electrode concentration states, $z_{1,j} = \bar{c}_{s,j}$ and $z_{2,j} = \bar{c}_{e,j}$, $j = \{n, p\}$, is investigated with respect to three parameters: a) solid phase diffusion $D^{eff}_{s,j}$, b) interface reaction rate constant k^*_j, and c) maximum lithium storage concentration $c_{s,max,j}$. The first two parameters are chosen because they represent the transport processes in the active particles. The third parameter is chosen because it enables determination of the electrode half cell potential.

$c_{s,max,j}$ is a fundamental property that is considered during the design of the battery electrode. The parameters $D^{eff}_{s,j}$ and k^*_j are also important in the context of SOC estimation and state-of-health (SOH) prognosis. The concentration dynamics which quantify the half cell potential are strongly dictated by diffusion within the active particles. With aging, active particle diffusion can be affected by factors such as electrode contamination and structural changes. The reaction-rate constant can be impacted by aging mechanisms such as the solid-electrolyte-interface layer growth. Therefore, as these parameters change with aging, sensitivity studies are very valuable in assessing how the output is manipulated by these factors. These parameters are represented by the vector $\theta_{i,j}$, where $i = \{1, 2, 3\}$:

$$[\theta_{1,j}\,\theta_{2,j}\,\theta_{3,j}]^T = [D^{eff}_{s,j}\;k^*_j\;c_{s,max,j}]^T \tag{11}$$

The sensitivity functions are defined as:

$$\begin{aligned} S_{1,1,j} &= \frac{\partial z_{1,j}}{\partial \theta_{1,j}},\;\; S_{1,2,j} = \frac{\partial z_{1,j}}{\partial \theta_{2,j}},\;\; S_{1,3,j} = \frac{\partial z_{1,j}}{\partial \theta_{3,j}}, \\ S_{2,1,j} &= \frac{\partial z_{2,j}}{\partial \theta_{1,j}},\;\; S_{2,2,j} = \frac{\partial z_{2,j}}{\partial \theta_{2,j}},\;\; S_{2,3,j} = \frac{\partial z_{2,j}}{\partial \theta_{3,j}}, \end{aligned} \tag{12}$$

where $z_{1,j} = z_{1,j}(x, u, t, \theta_j)$, and $z_{2,j} = z_{2,j}(x, u, t, \theta_j)$. The variable u represents I_{app} and the variable x represents the Cartesian direction along the electrode thickness. The state equations are:

$$\begin{aligned} \frac{\partial z_{1,j}}{\partial t} &= D^{eff}_{s,j}\frac{\partial^2 z_{1,j}}{\partial x^2} - \frac{1}{F}J_{Li,j} = f_{1,j}\,, \\ \frac{\partial z_{2,j}}{\partial t} &= \frac{1}{\eta_{e,j}}\left(D^{eff}_{e,j}\frac{\partial^2 z_{2,j}}{\partial x^2} + \frac{RTt^2_+}{F^2}K^{eff}_{e,j}\frac{\partial^2 \ln z_{2,j}}{\partial x^2}\right. \\ &\quad \left. + \frac{t_+}{F}K^{eff}_{e,j}\frac{\partial^2 \bar{\phi}_{e,j}}{\partial x^2} + \frac{1}{F}J_{Li,j}\right) = f_{2,j}\,, \end{aligned} \tag{13}$$

where $f_{1,j} = f_{1,j}(z_{1,j}, z_{2,j}, u, \theta_j)$ and $f_{2,j} = f_{2,j}(z_{1,j}, z_{2,j}, u, \theta_j)$.

The sensitivity equations of $z_{1,j}$ and $z_{2,j}$ are formulated by taking the partial derivative of the state equations with respect to $\theta_{i,j}$:

$$\begin{aligned} \frac{\partial}{\partial \theta_{i,j}}\left(\frac{\partial z_{1,j}}{\partial t}\right) &= \frac{\partial}{\partial t}\left(\frac{\partial z_{1,j}}{\partial \theta_{i,j}}\right) = \frac{\partial f_{1,j}(z_{1,j}, z_{2,j}, u, \theta_{i,j})}{\partial \theta_{i,j}} \\ &= \frac{\partial f_{1,j}}{\partial z_{1,j}}\frac{\partial z_{1,j}}{\partial \theta_{i,j}} + \frac{\partial f_{1,j}}{\partial z_{2,j}}\frac{\partial z_{2,j}}{\partial \theta_{i,j}} + \frac{\partial f_{1,j}}{\partial u}\frac{\partial u}{\partial \theta_{i,j}} + \frac{\partial f_{1,j}}{\partial \theta_{i,j}}\,, \\ \frac{\partial}{\partial \theta_{i,j}}\left(\frac{\partial z_{2,j}}{\partial t}\right) &= \frac{\partial}{\partial t}\left(\frac{\partial z_{2,j}}{\partial \theta_{i,j}}\right) = \frac{\partial f_{2,j}(z_{1,j}, z_{2,j}, u, \theta_{i,j})}{\partial \theta_{i,j}} \\ &= \frac{\partial f_{2,j}}{\partial z_{1,j}}\frac{\partial z_{1,j}}{\partial \theta_{i,j}} + \frac{\partial f_{2,j}}{\partial z_{2,j}}\frac{\partial z_{2,j}}{\partial \theta_{i,j}} + \frac{\partial f_{2,j}}{\partial u}\frac{\partial u}{\partial \theta_{i,j}} + \frac{\partial f_{2,j}}{\partial \theta_{i,j}} \end{aligned} \tag{14}$$

Since u is an independent variable, its partial derivative with respect to $\theta_{i,j}$ is equal to zero. Therefore, the sensitivity equations are reduced to:

$$\begin{aligned} \frac{\partial}{\partial t}\left(\frac{\partial z_{1,j}}{\partial \theta_{i,j}}\right) &= \frac{\partial f_{1,j}}{\partial z_{1,j}}\frac{\partial z_{1,j}}{\partial \theta_{i,j}} + \frac{\partial f_{1,j}}{\partial z_{2,j}}\frac{\partial z_{2,j}}{\partial \theta_{i,j}} + \frac{\partial f_{1,j}}{\partial \theta_{i,j}}\,, \\ \frac{\partial}{\partial t}\left(\frac{\partial z_{2,j}}{\partial \theta_{i,j}}\right) &= \frac{\partial f_{2,j}}{\partial z_{1,j}}\frac{\partial z_{1,j}}{\partial \theta_{i,j}} + \frac{\partial f_{2,j}}{\partial z_{2,j}}\frac{\partial z_{2,j}}{\partial \theta_{i,j}} + \frac{\partial f_{2,j}}{\partial \theta_{i,j}} \end{aligned} \tag{15}$$

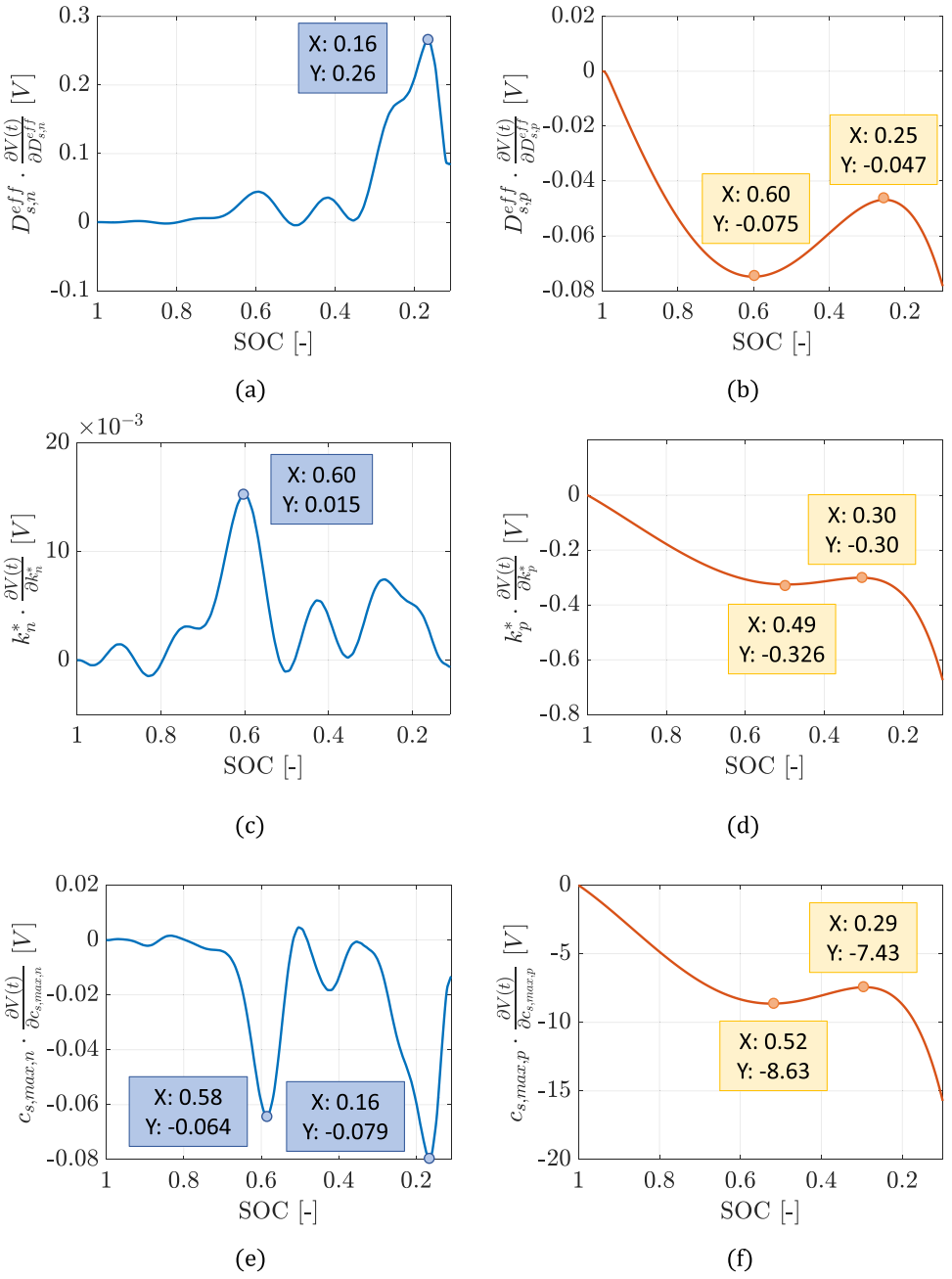

Figure 9. Results from the sensitivity studies, quantifying the influence on the output voltage, $V(t)$, due to the: (a) anode and (b) cathode electrode diffusivity coefficient, $D_{s,j}^{eff}$, (c) anode and (d) cathode reaction rate constant, k_j^*, (e) anode and (f) cathode maximum lithium storage concentration, $c_{s,max,j}$ parameters.

If the nominal values of $\theta_{i,j}$ are represented by $\theta_{i,j,0}$, then for values of $\theta_{i,j}$ sufficiently close to $\theta_{i,j,0}$, the sensitivity functions $\left.\frac{\partial z_{1,j}}{\partial \theta_{i,j}}\right|_{\theta_{i,j}=\theta_{i,j,0}}$ and $\left.\frac{\partial z_{2,j}}{\partial \theta_{i,j}}\right|_{\theta_{i,j}=\theta_{i,j,0}}$ are unique solutions of the following equations:

$$\begin{bmatrix}\dot{S}_{1,i,j}\\ \dot{S}_{2,i,j}\end{bmatrix} = \begin{bmatrix}\frac{\partial f_{1,j}}{\partial z_{1,j}} & \frac{\partial f_{1,j}}{\partial z_{2,j}}\\ \frac{\partial f_{2,j}}{\partial z_{1,j}} & \frac{\partial f_{2,j}}{\partial z_{2,j}}\end{bmatrix}_{\theta_{i,j,0}} \begin{bmatrix}S_{1,i,j}\\ S_{2,i,j}\end{bmatrix} + \begin{bmatrix}\frac{\partial f_{1,j}}{\partial \theta_{i,j}}\\ \frac{\partial f_{2,j}}{\partial \theta_{i,j}}\end{bmatrix}; \; \begin{matrix}S_{1,i,j}(t_0)=0\\ S_{2,i,j}(t_0)=0\end{matrix} \quad [16]$$

To solve the sensitivity equations, the Jacobian matrices

$$A_j(t,\theta_{i,j,0}) = \left.\frac{\partial f_j(z_j,u,t,\theta_{i,j})}{\partial z_j}\right|_{z_j=z_j(x,u,t,\theta_{i,j,0}),\theta_{i,j}=\theta_{i,j,0}} \quad [17]$$

and

$$B_j(t,\theta_{i,j,0}) = \left.\frac{\partial f_j(z_j,u,t,\theta_{i,j})}{\partial \theta_{i,j}}\right|_{z_j=z_j(x,u,t,\theta_{i,j,0}),\theta_{i,j}=\theta_{i,j,0}}, \quad [18]$$

where $f_j = [f_{1,j}\, f_{2,j}]^T$ and $z_j = [z_{1,j}\, z_{2,j}]^T$, must be first evaluated. The system of sensitivity equations are:

$$\begin{bmatrix}\dot{S}_{1,1,j} & \dot{S}_{1,2,j} & \dot{S}_{1,3,j}\\ \dot{S}_{2,1,j} & \dot{S}_{2,2,j} & \dot{S}_{2,3,j}\end{bmatrix} = \begin{bmatrix}\frac{\partial f_{1,j}}{\partial z_{1,j}} & \frac{\partial f_{1,j}}{\partial z_{2,j}}\\ \frac{\partial f_{2,j}}{\partial z_{1,j}} & \frac{\partial f_{2,j}}{\partial z_{2,j}}\end{bmatrix}_{\theta_{i,j,0}} \begin{bmatrix}S_{1,1,j} & S_{1,2,j} & S_{1,3,j}\\ S_{2,1,j} & S_{2,2,j} & S_{2,3,j}\end{bmatrix}$$

$$+ \begin{bmatrix}\frac{\partial f_{1,j}}{\partial \theta_{1,j}} & \frac{\partial f_{1,j}}{\partial \theta_{2,j}} & \frac{\partial f_{1,j}}{\partial \theta_{3,j}}\\ \frac{\partial f_{2,j}}{\partial \theta_{1,j}} & \frac{\partial f_{2,j}}{\partial \theta_{2,j}} & \frac{\partial f_{2,j}}{\partial \theta_{3,j}}\end{bmatrix} \quad [19]$$

with initial conditions $S_{1,i,j}(t_0) = 0$; $S_{2,i,j}(t_0) = 0$. The sensitivity equations are resolved for the 23°C 1 C-rate data. The identified parameters at the end of Step 1 were used as nominal values. The boundary conditions for the sensitivity functions are summarized in Table VIII.

The sensitivity functions are used to determine the impact of parameters on $V(t)$:

$$\frac{\partial V(t)}{\partial \theta_{i,j}} = \left.\frac{\partial \bar{\phi}_{s,p}(t)}{\partial \theta_{i,j}}\right|_{x=L_{cell}} - \left.\frac{\partial \bar{\phi}_{s,n}(t)}{\partial \theta_{i,j}}\right|_{x=0}, \quad i = 1, 2, 3 \qquad [20]$$

The parameters $\theta_{i,n}$ are defined only in the anode domain. The same applies for the cathode parameters $\theta_{i,p}$. Therefore, the partial derivatives $\left.\frac{\partial \bar{\phi}_{s,p}(t)}{\partial \theta_{i,n}}\right|_{x=L_{cell}}$ and $\left.\frac{\partial \bar{\phi}_{s,n}(t)}{\partial \theta_{i,p}}\right|_{x=0}$ are equal to 0. The sensitivity of $V(t)$ is then equal to:

$$\frac{\partial V(t)}{\partial \theta_{i,n}} = -\left(\frac{\partial \bar{\phi}_{s,n}(t)}{\partial \bar{c}_{s,n}}\right) \cdot \left(\frac{\partial \bar{c}_{s,n}}{\partial \theta_{i,n}}\right)\Bigg|_{x=0}, \quad i = 1, 2, 3 \qquad [21]$$

with respect to the anode parameters and

$$\frac{\partial V(t)}{\partial \theta_{i,p}} = \left(\frac{\partial \bar{\phi}_{s,p}(t)}{\partial \bar{c}_{s,p}}\right) \cdot \left(\frac{\partial \bar{c}_{s,p}}{\partial \theta_{i,p}}\right)\Bigg|_{x=L_{cell}}, \quad i = 1, 2, 3 \qquad [22]$$

with respect to the cathode parameters. The partial derivative of $\bar{\phi}_{s,j}$ with respect to $\bar{c}_{s,j}$ is obtained by solving the following PDE in the respective electrodes:

$$K_{s,j}^{eff} \cdot \frac{\partial^2}{\partial x^2}\left(\frac{\partial \bar{\phi}_{s,j}}{\partial \bar{c}_{s,j}}\right) = \frac{\partial J_{Li,j}}{\partial \bar{c}_{s,j}}, \qquad [23]$$

subject to the boundary conditions:

$$\frac{\partial}{\partial x}\left(\frac{\partial \bar{\phi}_{s,j}}{\partial \bar{c}_{s,j}}\right)\Bigg|_{x=\{0,L_n,L_n+L_s,L_{cell}\}} = 0 \qquad [24]$$

Results.—The results of the sensitivity studies are illustrated in Fig. 9 in the cell SOC range of [0.1,1]. The sensitivity functions are normalized in units of [V] for comparison. The main inference deduced from these plots are:

(1) Fig. 9a indicates that for a constant current discharge, the sensitivity of $V(t)$ to $D_{s,n}^{eff}$ is the highest at SOC of 16%, which can be categorized in the low SOC region. On the other hand, in Fig. 9b, the overall output voltage sensitivity to $D_{s,p}^{eff}$ increases with decreasing SOC in the cathode. This means that using a constant current discharge input, the identification of the diffusion parameters is most effective toward the end of discharge.

(2) Fig. 9c shows that $V(t)$ is most sensitive to k_n^* at around SOC equals to 60%. This indicates that incorrect values of this parameter may result in higher prediction error in voltage at this SOC. Fig. 9d shows that there is an increasing trend in the sensitivity of $V(t)$ to k_p^* with decreasing SOC. Moreover, in the SOC range of 50% to 30% this sensitivity function is almost flat, suggesting a lack of sensitivity over this SOC range. As such, it is best to identify this parameter either at high SOC (from 100% unitl 50%) or at low cell SOC.

(3) In Fig. 9e, $V(t)$ is most sensitive to $c_{s,max,n}$ at medium and low SOC levels. This implies that for a constant current input profile, these parameters are best identified at those two critical SOC values. Fig. 9f reiterates the same observation that we have made above for the other cathode sensitivity functions.

Conclusions

For the first time, we have provided an approach that correlates the impact of key lithium transport parameters with the states of the FHM model. Accurate identification of the diffusion and reaction rate parameters is crucial since their variation influences model-based estimation of SOC and SOH. Using the sensitivity functions, we determine how the voltage is dependent on parameters as a function of SOC for a constant current input profile. Since the parameter $c_{s,max,n}$ influences the voltage at medium and low SOC, there is more confidence in retaining its identified value for reduced-order models formulated from the FHM model. A reliable identification of the electrode diffusion parameters is possible using experimental data that majorly retrieves voltage information from low SOC operation. In future work, we will investigate different current inputs, operating SOC range, and temperature conditions to analyze the impact of parameters on the output voltage. Using this information, we can create parameter subsets for efficient identification.

This work also identifies that under high temperatures of battery operation and a nominal discharge current,the DFN model suffers a loss in its voltage predictability at low cell SOC. The model validation results using different 23°C discharge data sets infer an overall better performance of the FHM model, and that caution must be exercised while using the DFN model for applications where the battery operates at low SOC regimes.

The effective ionic transport properties for all the results presented in this work have been based on the standard Bruggeman relationship for the DFN model, and the closure approach for the FHM model. In this work, we considered the electrodes to be composed of perfectly spherical active particles. However, recent publications[39,40]

Table AI. $U_{0,n}$ and its partial derivative with respect to $\bar{c}_{s,n}$.

Term	Mathematical Expression
$U_{0,n}$	$-4.6\times10^{10}\left(\frac{\bar{c}_{s,n}}{c_{s,max,n}}\right)^{24} + 4.86\times10^{11}\left(\frac{\bar{c}_{s,n}}{c_{s,max,n}}\right)^{23} - 2.32\times10^{12}\left(\frac{\bar{c}_{s,n}}{c_{s,max,n}}\right)^{22} + 6.51\times10^{12}\left(\frac{\bar{c}_{s,n}}{c_{s,max,n}}\right)^{21} -$ $1.15\times10^{13}\left(\frac{\bar{c}_{s,n}}{c_{s,max,n}}\right)^{20} + 1.16\times10^{13}\left(\frac{\bar{c}_{s,n}}{c_{s,max,n}}\right)^{19} - 1.37\times10^{12}\left(\frac{\bar{c}_{s,n}}{c_{s,max,n}}\right)^{18} - 1.72\times10^{13}\left(\frac{\bar{c}_{s,n}}{c_{s,max,n}}\right)^{17} +$ $3.42\times10^{13}\left(\frac{\bar{c}_{s,n}}{c_{s,max,n}}\right)^{16} - 4\times10^{13}\left(\frac{\bar{c}_{s,n}}{c_{s,max,n}}\right)^{15} + 3.38\times10^{13}\left(\frac{\bar{c}_{s,n}}{c_{s,max,n}}\right)^{14} - 2.18\times10^{13}\left(\frac{\bar{c}_{s,n}}{c_{s,max,n}}\right)^{13} +$ $1.1\times10^{13}\left(\frac{\bar{c}_{s,n}}{c_{s,max,n}}\right)^{12} - 4.41\times10^{12}\left(\frac{\bar{c}_{s,n}}{c_{s,max,n}}\right)^{11} + 1.4\times10^{14}\left(\frac{\bar{c}_{s,n}}{c_{s,max,n}}\right)^{10} - 3.52\times10^{11}\left(\frac{\bar{c}_{s,n}}{c_{s,max,n}}\right)^{9} +$ $6.95\times10^{10}\left(\frac{\bar{c}_{s,n}}{c_{s,max,n}}\right)^{8} - 1.06\times10^{10}\left(\frac{\bar{c}_{s,n}}{c_{s,max,n}}\right)^{7} + 1.24\times10^{9}\left(\frac{\bar{c}_{s,n}}{c_{s,max,n}}\right)^{6} - 1.06\times10^{8}\left(\frac{\bar{c}_{s,n}}{c_{s,max,n}}\right)^{5}$ $+6.57\times10^{6}\left(\frac{\bar{c}_{s,n}}{c_{s,max,n}}\right)^{4} - 2.78\times10^{5}\left(\frac{\bar{c}_{s,n}}{c_{s,max,n}}\right)^{3} + 7.67\times10^{3}\left(\frac{\bar{c}_{s,n}}{c_{s,max,n}}\right)^{2} - 131.06\left(\frac{\bar{c}_{s,n}}{c_{s,max,n}}\right) + 1.4367$
$\frac{\partial U_{0,n}}{\partial \bar{c}_{s,n}}$	$-\frac{1.1\times10^{12}}{c_{s,max,n}}\left(\frac{\bar{c}_{s,n}}{c_{s,max,n}}\right)^{23} + \frac{1.12\times10^{13}}{c_{s,max,n}}\left(\frac{\bar{c}_{s,n}}{c_{s,max,n}}\right)^{22} - \frac{5.11\times10^{13}}{c_{s,max,n}}\left(\frac{\bar{c}_{s,n}}{c_{s,max,n}}\right)^{21} + \frac{1.37\times10^{14}}{c_{s,max,n}}\left(\frac{\bar{c}_{s,n}}{c_{s,max,n}}\right)^{20} - \frac{2.29\times10^{14}}{c_{s,max,n}}\left(\frac{\bar{c}_{s,n}}{c_{s,max,n}}\right)^{19} + \frac{2.2\times10^{14}}{c_{s,max,n}}\left(\frac{\bar{c}_{s,n}}{c_{s,max,n}}\right)^{18} -$ $\frac{2.47\times10^{13}}{c_{s,max,n}}\left(\frac{\bar{c}_{s,n}}{c_{s,max,n}}\right)^{17} - \frac{2.92\times10^{14}}{c_{s,max,n}}\left(\frac{\bar{c}_{s,n}}{c_{s,max,n}}\right)^{16} + \frac{5.47\times10^{14}}{c_{s,max,n}}\left(\frac{\bar{c}_{s,n}}{c_{s,max,n}}\right)^{15} - \frac{6.01\times10^{14}}{c_{s,max,n}}\left(\frac{\bar{c}_{s,n}}{c_{s,max,n}}\right)^{14} + \frac{4.73\times10^{14}}{c_{s,max,n}}\left(\frac{\bar{c}_{s,n}}{c_{s,max,n}}\right)^{13} - \frac{2.83\times10^{14}}{c_{s,max,n}}\left(\frac{\bar{c}_{s,n}}{c_{s,max,n}}\right)^{12} +$ $\frac{1.32\times10^{14}}{c_{s,max,n}}\left(\frac{\bar{c}_{s,n}}{c_{s,max,n}}\right)^{11} - \frac{4.85\times10^{13}}{c_{s,max,n}}\left(\frac{\bar{c}_{s,n}}{c_{s,max,n}}\right)^{10} + \frac{1.4\times10^{13}}{c_{s,max,n}}\left(\frac{\bar{c}_{s,n}}{c_{s,max,n}}\right)^{9} - \frac{3.17\times10^{12}}{c_{s,max,n}}\left(\frac{\bar{c}_{s,n}}{c_{s,max,n}}\right)^{8} + \frac{5.56\times10^{11}}{c_{s,max,n}}\left(\frac{\bar{c}_{s,n}}{c_{s,max,n}}\right)^{7} - \frac{7.44\times10^{10}}{c_{s,max,n}}\left(\frac{\bar{c}_{s,n}}{c_{s,max,n}}\right)^{6} +$ $\frac{7.41\times10^{9}}{c_{s,max,n}}\left(\frac{\bar{c}_{s,n}}{c_{s,max,n}}\right)^{5} - \frac{5.32\times10^{8}}{c_{s,max,n}}\left(\frac{\bar{c}_{s,n}}{c_{s,max,n}}\right)^{4} + \frac{2.63\times10^{7}}{c_{s,max,n}}\left(\frac{\bar{c}_{s,n}}{c_{s,max,n}}\right)^{3} - \frac{8.34\times10^{5}}{c_{s,max,n}}\left(\frac{\bar{c}_{s,n}}{c_{s,max,n}}\right)^{2} + \frac{1.53\times10^{4}}{c_{s,max,n}}\left(\frac{\bar{c}_{s,n}}{c_{s,max,n}}\right) - \frac{131.06}{c_{s,max,n}}$

Table AII. The partial derivative of $U_{0,n}$ with respect to $c_{s,max,n}$.

Term	Mathematical Expression
$\frac{\partial U_{0,n}}{\partial c_{s,max,n}}$	$\frac{1.1\times10^{12}}{c_{s,max,n}}\left(\frac{\bar{c}_{s,n}}{c_{s,max,n}}\right)^{24} - \frac{1.12\times10^{13}}{c_{s,max,n}}\left(\frac{\bar{c}_{s,n}}{c_{s,max,n}}\right)^{23} + \frac{5.11\times10^{13}}{c_{s,max,n}}\left(\frac{\bar{c}_{s,n}}{c_{s,max,n}}\right)^{22} - \frac{1.37\times10^{14}}{c_{s,max,n}}\left(\frac{\bar{c}_{s,n}}{c_{s,max,n}}\right)^{21} + \frac{2.29\times10^{14}}{c_{s,max,n}}\left(\frac{\bar{c}_{s,n}}{c_{s,max,n}}\right)^{20} - \frac{2.2\times10^{14}}{c_{s,max,n}}\left(\frac{\bar{c}_{s,n}}{c_{s,max,n}}\right)^{19} + \frac{2.47\times10^{13}}{c_{s,max,n}}\left(\frac{\bar{c}_{s,n}}{c_{s,max,n}}\right)^{18} + \frac{2.92\times10^{14}}{c_{s,max,n}}\left(\frac{\bar{c}_{s,n}}{c_{s,max,n}}\right)^{17} - \frac{5.47\times10^{14}}{c_{s,max,n}}\left(\frac{\bar{c}_{s,n}}{c_{s,max,n}}\right)^{16} + \frac{6.01\times10^{14}}{c_{s,max,n}}\left(\frac{\bar{c}_{s,n}}{c_{s,max,n}}\right)^{15} - \frac{4.73\times10^{14}}{c_{s,max,n}}\left(\frac{\bar{c}_{s,n}}{c_{s,max,n}}\right)^{14} + \frac{2.83\times10^{14}}{c_{s,max,n}}\left(\frac{\bar{c}_{s,n}}{c_{s,max,n}}\right)^{13} - \frac{1.32\times10^{14}}{c_{s,max,n}}\left(\frac{\bar{c}_{s,n}}{c_{s,max,n}}\right)^{12} + \frac{4.85\times10^{13}}{c_{s,max,n}}\left(\frac{\bar{c}_{s,n}}{c_{s,max,n}}\right)^{11} - \frac{1.4\times10^{13}}{c_{s,max,n}}\left(\frac{\bar{c}_{s,n}}{c_{s,max,n}}\right)^{10} + \frac{3.17\times10^{12}}{c_{s,max,n}}\left(\frac{\bar{c}_{s,n}}{c_{s,max,n}}\right)^{9} - \frac{5.56\times10^{11}}{c_{s,max,n}}\left(\frac{\bar{c}_{s,n}}{c_{s,max,n}}\right)^{8} + \frac{7.44\times10^{10}}{c_{s,max,n}}\left(\frac{\bar{c}_{s,n}}{c_{s,max,n}}\right)^{7} - \frac{7.41\times10^{9}}{c_{s,max,n}}\left(\frac{\bar{c}_{s,n}}{c_{s,max,n}}\right)^{6} + \frac{5.32\times10^{8}}{c_{s,max,n}}\left(\frac{\bar{c}_{s,n}}{c_{s,max,n}}\right)^{5} - \frac{2.63\times10^{7}}{c_{s,max,n}}\left(\frac{\bar{c}_{s,n}}{c_{s,max,n}}\right)^{4} + \frac{8.34\times10^{5}}{c_{s,max,n}}\left(\frac{\bar{c}_{s,n}}{c_{s,max,n}}\right)^{3} - \frac{1.53\times10^{4}}{c_{s,max,n}}\left(\frac{\bar{c}_{s,n}}{c_{s,max,n}}\right)^{2} + \frac{131.06}{c_{s,max,n}}\left(\frac{\bar{c}_{s,n}}{c_{s,max,n}}\right)$

have introduced approaches that extract effective transport parameters for the DFN model based on microstructural images obtained from the X-ray computed tomography technique. Model performance can be enhanced by utilizing such pore-scale information. We are currently investigating the extension of the closure approach for obtaining effective transport properties using scanning electron microscopic images of the anode and cathode. Future work will involve simulation and optimization studies on the DFN and FHM models based on electrochemical properties obtained from realistic electrode morphologies.

Acknowledgments

The authors acknowledge the partial support of the National Science Foundation through the grant CAREER #1839050. The authors would also like to thank the anonymous reviewer whose suggestions have contributed to the enhancement of our manuscript.

Appendix A: Sensitivity Analysis: Anode Equations

The anode open circuit potential, $U_{0,n}$, was obtained from experimental measurements.[41] To obtain a continuously partially differentiable expression for $U_{0,n}$, a 24^{th} order polynomial fit was applied to this data. The polynomial expression for $U_{0,n}$, and the partial derivative of $U_{0,n}$ with respect to $\bar{c}_{s,n}$ and $c_{s,max,n}$ obtained using this relationship, are presented in Tables AI and AII. The plot for $U_{0,n}$ as a function of $\frac{\bar{c}_{s,n}}{c_{s,max,n}}$, and the plots for $\frac{\partial U_{0,n}}{\partial \bar{c}_{s,n}}$ and $\frac{\partial U_{0,n}}{\partial c_{s,max,n}}$ as a function of $\frac{\bar{c}_{s,n}}{c_{s,max,n}}$ around the nominal value of $c_{s,max,n}$ are illustrated in Fig. AI.

Appendix B: Sensitivity Analysis: Cathode Equations

A 4^{th} order polynomial expression for the cathode open circuit potential, $U_{0,p}$, obtained by applying a fit to experimental measurements,[43] has been provided in Ref. 42 The polynomial expression for $U_{0,p}$, and the partial derivative of $U_{0,p}$ with respect to $\bar{c}_{s,p}$ and $c_{s,max,p}$ are presented in Table BI. The plot for $U_{0,p}$ as a function of $\frac{\bar{c}_{s,p}}{c_{s,max,p}}$, and the plots for $\frac{\partial U_{0,p}}{\partial \bar{c}_{s,p}}$ and $\frac{\partial U_{0,p}}{\partial c_{s,max,p}}$ as a function of $\frac{\bar{c}_{s,p}}{c_{s,max,p}}$ around the nominal value of $c_{s,max,p}$ are illustrated in Fig. BI.

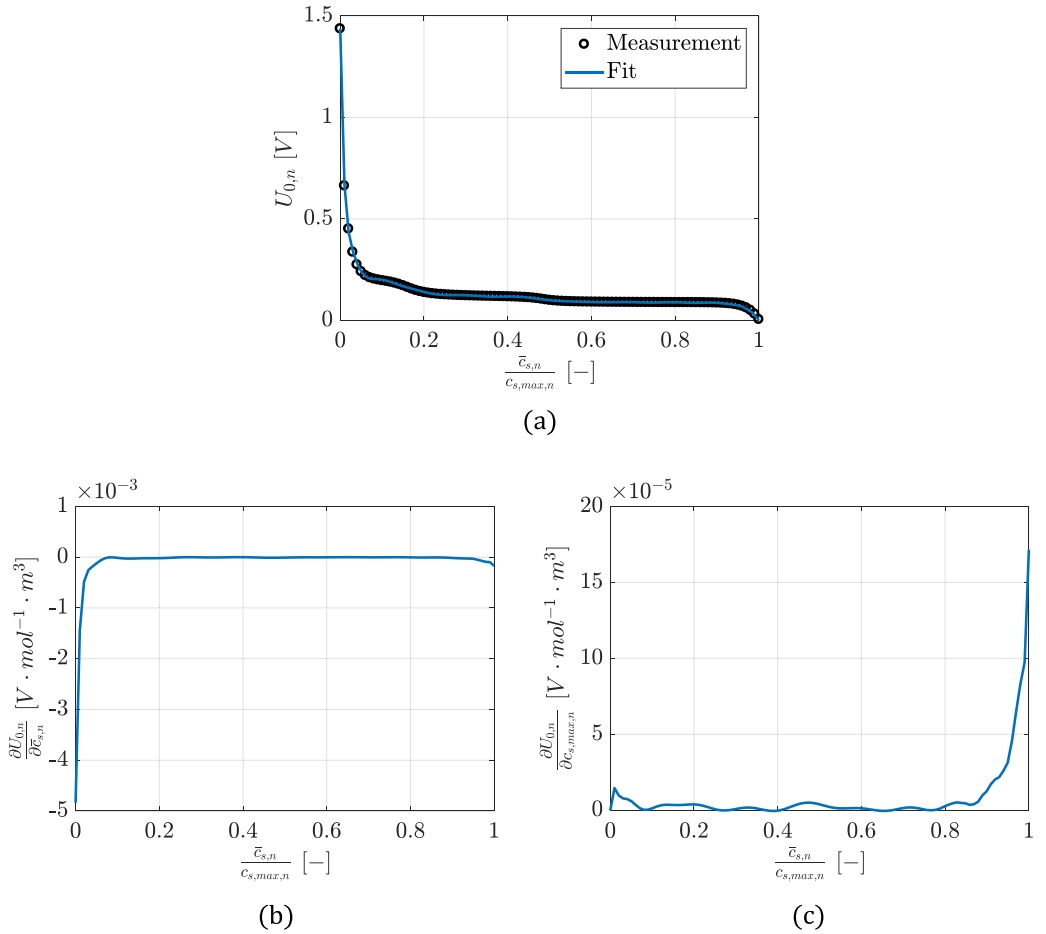

Figure AI. $U_{0,n}$ and its partial derivatives $\frac{\partial U_{0,n}}{\partial \bar{c}_{s,n}}$ and $\frac{\partial U_{0,n}}{\partial c_{s,max,n}}$ as a function of $\frac{\bar{c}_{s,n}}{c_{s,max,n}}$. The partial derivatives are evaluated around the nominal value of $c_{s,max,n}$. A polynomial expression for $U_{0,n}$ was obtained by applying a fit to experimental measurements.[41]

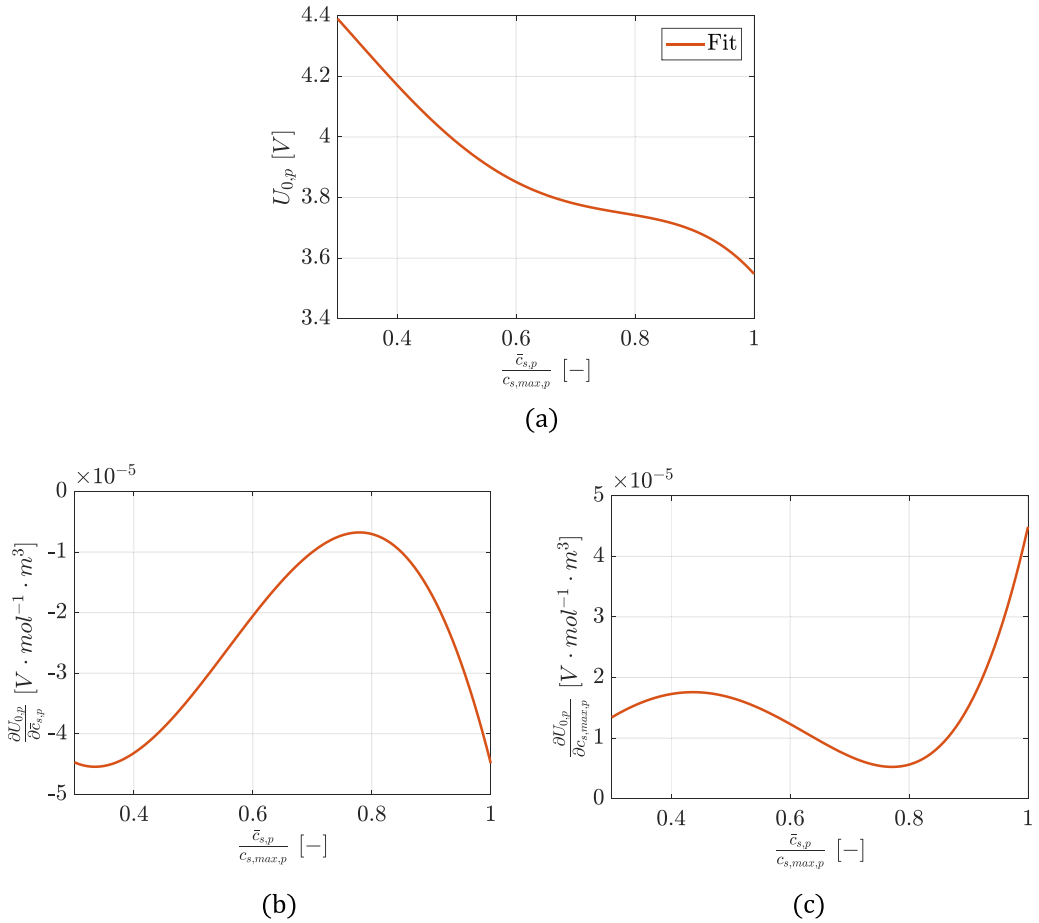

Figure BI. $U_{0,p}$ and its partial derivatives $\frac{\partial U_{0,p}}{\partial \bar{c}_{s,p}}$ and $\frac{\partial U_{0,p}}{\partial c_{s,max,p}}$ as a function of $\frac{\bar{c}_{s,p}}{c_{s,max,p}}$. The partial derivatives are evaluated around the nominal value of $c_{s,max,p}$. The curve for $U_{0,p}$ is plotted using the polynomial expression provided in Ref. 42, which in turn was obtained by applying a polynomial fit to experimental measurements.[43]

Table BI. $U_{0,p}$ and its partial derivatives with respect to $\bar{c}_{s,p}$ and $c_{s,max,p}$.

Term	Mathematical Expression
$U_{0,p}$	$-10.72 \cdot \left(\frac{\bar{c}_{s,p}}{c_{s,max,p}}\right)^4 + 23.88 \cdot \left(\frac{\bar{c}_{s,p}}{c_{s,max,p}}\right)^3 - 16.77 \cdot \left(\frac{\bar{c}_{s,p}}{c_{s,max,p}}\right)^2 + 2.595 \cdot \left(\frac{\bar{c}_{s,p}}{c_{s,max,p}}\right) + 4.563$
$\frac{\partial U_{0,p}}{\partial \bar{c}_{s,p}}$	$\frac{-42.88}{c_{s,max,p}} \cdot \left(\frac{\bar{c}_{s,p}}{c_{s,max,p}}\right)^3 + \frac{71.64}{c_{s,max,p}} \cdot \left(\frac{\bar{c}_{s,p}}{c_{s,max,p}}\right)^2 - \frac{33.54}{c_{s,max,p}} \cdot \left(\frac{\bar{c}_{s,p}}{c_{s,max,p}}\right) + \frac{2.595}{c_{s,max,p}}$
$\frac{\partial U_{0,p}}{\partial c_{s,max,p}}$	$\frac{42.88}{c_{s,max,p}} \cdot \left(\frac{\bar{c}_{s,p}}{c_{s,max,p}}\right)^4 - \frac{71.64}{c_{s,max,p}} \cdot \left(\frac{\bar{c}_{s,p}}{c_{s,max,p}}\right)^3 + \frac{33.64}{c_{s,max,p}} \cdot \left(\frac{\bar{c}_{s,p}}{c_{s,max,p}}\right)^2 - \frac{2.595}{c_{s,max,p}} \cdot \left(\frac{\bar{c}_{s,p}}{c_{s,max,p}}\right)$

List of Symbols

a_j	Electrode specific surface area, $[1/m]$
A_{cell}	Electrode cross-sectional area, $[m^2]$
$c_{s,j}$	Electrode concentration in the DFN model, $[mol/m^3]$
$c_{s,max,j}$	Electrode saturation concentration, $[mol/m^3]$
$c_{s,surf,j}$	Electrode surface concentration in the DFN model, $[mol/m^3]$
$\bar{c}_{e,j}$	Electrolyte average concentration, $[mol/m^3]$
$\bar{c}_{s,j}$	Electrode average concentration in the FHM model, $[mol/m^3]$
$D_{e,j}^{eff}$	Effective electrolyte diffusion coefficient, $[m^2/s]$
$D_{s,j}$	Active material diffusion coefficient in the DFN model, $[m^2/s]$
$D_{s,j}^{eff}$	Effective electrode diffusion coefficient in the FHM model, $[m^2/s]$
F	Faraday constant, $[Vs\Omega^{-1}mol^{-1}]$
I_{app}	Applied current, $[A]$
j	This suffix represents a property of the anode n, the separator s, or the cathode p
J_{Li}	Intercalation current density, $[A/m^3]$
k_j	Interface reaction rate constant in the DFN model, $[Am^{2.5}mol^{-1.5}]$
k_j^*	Interface reaction rate constant in the FHM model, $[A/mol]$
$K_{e,j}^{eff}$	Effective electrolyte conductivity coefficient, $[S^{-1}m^{-1}]$
$K_{s,j}^{eff}$	Effective electrode conductivity coefficient, $[S^{-1}m^{-1}]$
L_{cell}	Cumulative sum of the thickness of the anode, separator, and cathode, $[m]$
L_n	Thickness of the anode, $[m]$
L_p	Thickness of the cathode, $[m]$
L_s	Thickness of the separator, $[m]$
M_{opt}	Cost function
N	Total number of data samples used to evaluate the cost function, $[-]$
PSO	particle swarm optimization

Q_{cell}	Energy capacity of a lithium-ion cell, $[As]$
r	Radial coordinate direction from the center to the surface of each active particle, $[m]$
R	Universal gas constant, $[Jmol^{-1}K^{-1}]$
R_c	Contact resistance at the current collectors, $[\Omega]$
RMS	root mean square
t_+	Transference number, $[-]$
T	Cell temperature, $[K]$
x	Cartesian coordinate direction along the thickness of the electrodes, $[m]$
$x_{n,init}$	Initial anode stoichiometric coefficient, $[-]$
$x_{p,init}$	Initial cathode stoichiometric coefficient, $[-]$
$U_{0,j}$	Electrode open circuit potential, $[V]$
V_m	Experimentally measured cell terminal voltage, $[V]$
V_{model}	Model-predicted cell terminal voltage, $[V]$

Greek

$\eta_{e,j}$	Electrolyte volume fraction, $[-]$
$\eta_{s,j}$	Active material volume fraction, $[-]$
θ	Vector of identification parameters
$\bar{\phi}_{s,j}$	Averaged electrostatic potential in the active material phase of an electrode, $[V]$
$\bar{\phi}_{e,j}$	Averaged electrostatic potential in the electrolyte phase, $[V]$

ORCID

Harikesh Arunachalam https://orcid.org/0000-0003-0479-6686
Simona Onori https://orcid.org/0000-0002-6556-2608

References

1. A. Fotouhi, D. J. Auger, K. Propp, S. Longo, and M. Wild, "A review on electric vehicle battery modeling: From Lithium-ion toward Lithium-Sulphur," *Renewable and Sustainable Energy Reviews*, **56**, 1008 (2016).
2. G. Berckmans, M. Messagie, J. Smekens, N. Omar, L. Vanhaverbeke, and J. V. Mierlo, "Cost Projection of State of the Art Lithium-Ion Batteries for Electric Vehicles Up to 2030," *Energies*, **10**, 1 (2017).
3. J. W. Choi and D. Aurbach, "Promise and reality of post-lithium-ion batteries with high energy densities," *Nature Reviews Materials*, **1**, 16013 (2016).
4. R. E. Garcia, Y.-M. Chiang, W. C. Carter, P. Limthongkul, and C. M. Bishop, "Microstructural Modeling and Design of Rechargeable Lithium-Ion Batteries," *J. Electrochem. Soc.*, **152**(1), A255 (2005).
5. M. Doyle, T. F. Fuller, and J. Newman, "Modeling of Galvanostatic Charge and Discharge of the Lithium/Polymer/Insertion Cell," *J. Electrochem. Soc.*, **140**(6), 1526 (1993).
6. J. Tollefson, "Car industry: charging up the future," *Nature News*, **456**(7221), 436 (2008).
7. P. Albertus, J. Christensen, and J. Newman, "Experiments on and Modeling of Positive Electrodes with Multiple Active Materials for Lithium-Ion Batteries," *J. Electrochem. Soc.*, **156**(7), A606 (2009).
8. R. E. Garcia and Y-M. Chiang, "Spatially Resolved Modeling of Microstructurally Complex Battery Architectures," *J. Electrochem. Soc.*, **154**(9), A856 (2007).
9. F. Ciucci and W. Lai, "Derivation of Micro/Macro Lithium Battery Models from Homogenization," *Transp. Porous Med.*, **88**, 249 (2011).
10. B. Vijayaraghavan, D. R. Ely, Y-M. Chiang, R. G. Garcia, and R. E. Garcia, "An Analytical Method to Determine Tortuosity in Rechargeable Battery Electrodes," *J. Electrochem. Soc.*, **159**(5), A548 (2012).
11. D-W. Chung, P. R. Shearing, N. P. Brandon, S. J. Harris, and R. E. Garcia, "Particle Size Polydispersity in Li-Ion Batteries," *J. Electrochem. Soc.*, **161**(3), A422 (2014).
12. V. R. Subramanian, V. Boovaragavan, and V. D. Diwakar, "Toward Real-Time Simulation of Physics Based Lithium-Ion Battery Models," *Electrochemical and Solid State Letters*, **10**(11), A255 (2007).
13. S. Mazumder and J. Lu, "Faster-Than-Real-Time Simulation of Lithium Ion Batteries with Full Spatial and Temporal Resolution," *International Journal of Electrochemistry*, 268747, (2013).
14. V. R. Subramanian, V. Boovaragavan, V. Ramadesigan, and M. Arabandi, "Mathematical Model Reformulation for Lithium-Ion Battery Simulations: Galvanostatic Boundary Conditions," *J. Electrochem. Soc.*, **156**(4), A260 (2009).
15. L. Xia, E. Najafi, Z. Li, H. J. Bergveld, and M. C. F. Donkers, "A computationally efficient implementation of a full and reduced-order electrochemistry-based model for Li-ion batteries," *Applied Energy*, **208**, 1285 (2017).
16. J. L. Lee, A. Chemistruck, and G. L. Plett, "One-dimensional physics-based reduced-order model of lithium-ion dynamics," *J. Power Sources*, **220**, 430 (2012).
17. R. Klein, N. A. Chaturvedi, J. Christensen, J. Ahmed, R. Findeisen, and A. Kojic, "Electrochemical model based observer design for a lithium-ion battery," *IEEE Transactions on Control Systems Technology*, **21**(2), 289 (2013).
18. S. K. Rahimian, S. Rayman, and R. E. White, "Extension of physics-based single particle model for higher charge–discharge rates," *J. Power Sources*, **224**, 180 (2013).
19. H. Arunachalam and S. Onori, "What if the Doyle-Fuller-Newman model fails? A new macroscale modeling framework," *Proceedings of the 2018 Conference on Decision and Control*, 5702 (2018).
20. H. Arunachalam, S. Onori, and I. Battiato, "On Veracity of Macroscopic Lithium-Ion Battery Models," *J. Electrochem. Soc.*, **162**(10), A1940 (2015).
21. H. K. Khalil, *Nonlinear Systems*, 3rd Edition, New Jersey, Prentice Hall (2002).
22. H. Perez and S. J. Moura, "Sensitivity-Based Interval PDE Observer for Battery SOC Estimation," in *Proceedings of the 2015 American Control Conference*, pp. 323-328, IEEE (2015).
23. T.-S. Dao, C. P. Vyasarayani, and J. McPhee, "Simplification and order reduction of lithium-ion battery model based on porous-electrode theory," *J. Power Sources*, **198**, 329 (2012).
24. H. Arunachalam, S. Korneev, I. Battiato, and S. Onori, "Multiscale modeling approach to determine effective lithium-ion transport properties," in *Proceedings of the American Control Conference (ACC)*, pp. 92-97, IEEE, (2017).
25. L. O. Valoen and J. N. Reimers, "Transport Properties of $LiPF_6$-Based Li-Ion Battery Electrolytes," *J. Electrochem. Soc.*, **152**(5), A882 (2005).
26. M. Ebner, D. W. Chung, R. E. Garcia, and V. Wood, "Tortuosity Anisotropy in Lithium-Ion Battery Electrodes," *Advanced Energy Materials*, **4**(5), (2014).
27. G. L. Plett, Battery Management Systems, Volume I: Battery Modeling, *Artech House*, (2015).
28. H. Arunachalam, "A New Multiscale Modeling Framework for Lithium-Ion Battery Dynamics: Theory, Experiments, and Comparative Study with the Doyle-Fuller-Newman Model". PhD thesis, Clemson University, (2017).
29. Sony Energy Devices Corporation, "Lithium Ion Rechargeable Battery Technical Information". https://www.powerstream.com/p/us18650vtc4.pdf, (2012)
30. S. Ebbesen, P. Kiwitz, and L. Guzzella, "A generic particle swarm optimization matlab function," in *Proceedings of the American Control Conference (ACC)*, pp. 1519-1524, IEEE, (2012).
31. T. R. Tanim, C. D. Rahn, and C. Y. Wang, "State of charge estimation of a lithium ion cell based on a temperature dependent and electrolyte enhanced single particle model," *Energy*, **80**, 731 (2015).
32. L. Saw, Y. Ye, and A. A. O. Tay, "Electrochemical–thermal analysis of 18650 Lithium Iron Phosphate cell," *Energy Conversion and Management*, **75**, 162 (2013).
33. J. C. Forman, S. J. Moura, J. L. Stein, and H. K. Fathy, "Genetic identification and fisher identifiability analysis of the Doyle-Fuller-Newman model from experimental cycling of a $LiFePO_4$ cell," *J. Power Sources*, **210**, 263 (2012).
34. J. Li, L. Zou, F. Tian, X. Dong, Z. Zou, and H. Yang, "Parameter Identification of Lithium-Ion Batteries Model to Predict Discharge Behaviors Using Heuristic Algorithm," *J. Electrochem. Soc.*, **163**(8), A1646 (2016).
35. D. R. Baker and M. W. Verbrugge, "Intercalate diffusion in multiphase electrode materials and application to lithiated graphite," *J. Electrochem. Soc.*, **159**(8), A1341 (2012).
36. J. W. Kim, J. J. Travis, E. Hu, K.-W. Nam, S. C. Kim, C. S. Kang, J.-H. Woo, X.-Q. Yang, S. M. George, K. H. Oh et al., "Unexpected high power performance of atomic layer deposition coated $Li[Ni_{1/3}Mn_{1/3}Co_{1/3}]O_2$ cathodes," *J. Power Sources*, **254**, 190 (2014).
37. S. Yang, B. Yan, J. Wu, L. Lu, and K. Zeng, "Temperature-dependent lithium-ion diffusion and activation energy of Li1:2Co0:13Ni0:13Mn0:54O2 thin-film cathode at nanoscale by using electrochemical strain microscopy," *ACS Applied Materials & Interfaces*, **9**(16), 13999 (2017).
38. S. Cui, Y. Wei, T. Liu, W. Deng, Z. Hu, Y. Su, H. Li, M. Li, H. Guo, Y. Duan et al., "Optimized Temperature Effect of Li-Ion Diffusion with Layer Distance in $Li(Ni_xMn_yCo_z)O_2$ Cathode Materials for High Performance Li-Ion Battery," *Advanced Energy Materials*, **6**(4), 1501309 (2016).
39. B. L. Trembacki, A. N. Mistry, D. R. Noble, M. E. Ferraro, P. P. Mukherjee, and S. A. Roberts, "Mesoscale Analysis of Conductive Binder Domain Morphology in Lithium-Ion Battery Electrodes," *J. Electrochem. Soc.*, **165**(13), E725 (2018).
40. F. L. Usseglio-Viretta, A. Colclasure, A. N. Mistry, K. P. Y. Claver, F. Pouraghajan, D. P. Finegan, T. M. Heenan, D. Abraham, P. P. Mukherjee, D. Wheeler et al., "Resolving the Discrepancy in Tortuosity Factor Estimation for Li-Ion Battery Electrodes through Micro-Macro Modeling and Experiment," *J. Electrochem. Soc.*, **165**(14), A3403 (2018).
41. M. W. Verbrugge and B. J. Koch, "Electrochemical analysis of lithiated graphite anodes," *J. Electrochem. Soc.*, **150**(3), A374 (2003).
42. Y. Ji, Y. Zhang, and C.-Y. Wang, "Li-ion cell operation at low temperatures," *J. Electrochem. Soc.*, **160**(4), A636 (2013).
43. N. Yabuuchi, Y. Makimura, and T. Ohzuku, "Solid-State Chemistry and Electrochemistry of $LiCo_{1/3}Ni_{1/3}Mn_{1/3}O_2$ for Advanced lithium-ion batteries iii. rechargeable capacity and cycleability," *J. Electrochem. Soc.*, **154**(4), A314 (2007).